SELF-CROSSLINKING P(APM-*CO*-AA) USED IN BIOMIMETIC SCAFFOLDS

SELF-CROSSLINKING P(APM-*CO*-AA) MICROSTRUCTURED FILMS AND NANOFIBROUS SCAFFOLDS AS BIOMIMETIC SCAFFOLDS.

By CHRISTAL ZHOU, B. Sc.

A Thesis Submitted to the School of Graduate Studies in Partial Fulfilment of the Requirements for the Degree Master of Science

McMaster University MASTER OF SCIENCE (2017) Hamilton, Ontario (Chemical Biology)

TITLE: Self-crosslinking p(APM-*co*-AA) microstructured films and nanofibrous scaffolds as biomimetic scaffolds

AUTHOR: Christal Zhou, B. Sc. (McMaster University)

SUPERVISORS: Dr. Jose Moran-Mirabal and Dr. Harald D. H. Stöver

NUMBER OF PAGES: 99

LAY ABSTRACT

The extracellular matrix (ECM), present within all biological tissues, consists of 3-dimensional (3D) networks of proteins which provide chemical and physical cues for cells. Abnormalities in the ECM is associated with a variety of disorders, such as coronary heart disease and tumours. Thus, the study of the ECM and how it affects cell behaviour is important both for a better understanding of ECM-related diseases, as well as for creating ECM-mimics for tissue engineering. The goal of this thesis is to explore the fabrication of 3D scaffolds using a synthetic polyampholyte that can be crosslinked under heat and chemically tuned using functionalization. This polyampholyte was electrospun into nanofibers and prepared into microstructured films, which were used to study the effects of surface topography and chemistry on murine fibroblast morphology and attachment. These polyampholyte scaffolds provide a new means to study cell behaviour in environments that mimic certain aspects of the ECM.

ABSTRACT

In nature, cells reside within an extracellular matrix (ECM), consisting of 3-dimensional (3D) networks of collagen and elastin which provide biophysical/chemical signals to direct cellular development and behaviour. Traditional methods of studying cellular behaviour often involve using 2-dimensional *in vitro* models that are convenient and cost-effective, but may not be representative of 3D *in vivo* conditions. A synthetic polyampholyte system, poly(*N*-(3-aminopropyl)methacrylamide hydrochloride-*co*-acrylic acid) [p(APM-*co*-AA)], was used here for the first time to construct two types of 3-dimensionally structured cell supports to mimic the ECM: microstructured films and nanofibrous scaffolds. Microstructured films were fabricated using a shape-memory polymer structuring approach and nanofibrous scaffolds were formed using electrospinning. Both films and nanofibers were thermally crosslinked by reaction of initially formed anhydride groups with pendant amines. Film topography was tuned through polymer solution concentration, and the surface chemistry of the crosslinked p(APM-*co*-AA) scaffolds was tuned by reaction of residual anhydride groups with hydrophilic or hydrophobic amines. The effects of film surface topography and surface chemistry on fibroblast morphologies were explored using fluorescence microscopy. This work presents the fabrication and characterization of tunable, self-crosslinking p(APM-*co*-AA) scaffolds as promising ECM mimics.

ACKNOWLEDGEMENTS

I would like to sincerely thank my two excellent research supervisors, Dr. Jose Moran-Mirabal and Dr. Harald Stöver, for their constant guidance and support throughout this thesis project. Their ideas, enthusiasm, and patience throughout the years have made this project very enjoyable and exciting.

I am also very grateful for everyone in both the Dr. Stöver and Dr. Moran-Mirabal groups for their friendships and support during this project, especially Nicholas Burke, Jing Zhao, and Rachelle Kleinberger for teaching me polymer chemistry, Yujie Zhu for explaining fractal analysis, and Kevin Saem and Urooj Gill for their contributions to this work. I would also like to give special thanks to Alison Stewart, Sheilan Sinjari, Jennifer Wild, Lucia Lee, and Shanna Shi for supporting me and making this past year extremely memorable.

Many thanks to Tammy Feher for always being so helpful and the entire Chemistry and Chemical Biology department for their support. I would like to acknowledge McMaster University and NSERC for financial support.

Finally, I'd like to express my sincere gratitude to my family and friends, including Jake Fuller, who has supported me in all ways possible throughout my entire educational career.

TABLE OF CONTENTS

LIST OF FIGURES AND TABLES

Chapter 1:

Chapter 2:

Chapter 3:

LIST OF ALL ABBREVIATIONS AND SYMBOLS

extracellular matrix (ECM)
poly(*N*-(3-aminopropyl)methacrylamide hydrochloride-*co*-acrylic acid) [p(APM-*co*-AA)]
polystyrene (PS)
poly(lactic-*co*-glycolic acid) (PLGA)
poly(ε-caprolactone) (PCL)
polydimethylsiloxane (PDMS)
attenuated reflectance infrared spectroscopy (ATR IR)
scanning electron microscopy (SEM)
thermogravimetric analysis (TGA)
Dulbecco's Modified Eagle Medium (DMEM)
bovine calf serum (BCS)
poly(acrylic acid) (pAA)
bovine serum albumin (BSA)
fractal dimensions of perimeter (FDPs)
gel permeation chromatography (GPC)
4',6-Diamidino-2-Phenylindole, Dihydrochloride (DAPI)

DECLARATION OF ACADEMIC ACHIEVEMENT

Dr. Jose Moran-Mirabal and Dr. Harald Stöver, my supervisors, provided much guidance and advice on this entire project and editing all chapters of this thesis.

Chapter 2:

Jing Zhao, a colleague in the Dr. Stöver group, provided me with guidance in synthesizing the polyampholytes, as well as obtained and analyzed NMR spectra related to the syntheses. Kevin Saem and Urooj Gill, colleagues in the Dr. Moran-Mirabal group, obtained thermogravimetric analysis measurements and scanning electron microscopy images, and white light interferometry measurements respectively, while I analyzed the data. Yujie Zhu, from the Dr. Moran-Mirabal group, provided invaluable information on how to perform fractal analysis and statistical methodology for the cell morphology experiments. I was responsible for designing and carrying out experiments, analyzing and interpreting data, and writing the manuscript.

Chapter 3:

Kevin Saem provided me with training on the electrospinning set up. I was responsible for designing and carrying out experiments, analyzing and interpreting data, and writing the manuscript.

CHAPTER 1. INTRODUCTION

1.1 The extracellular matrix and its importance

The extracellular matrix (ECM), the non-cellular constituent within all tissues, provides cells with physical scaffolding as well as biochemical/biomechanical cues necessary for tissue morphogenesis and differentiation.[1] The ECM guides the morphological organization and physiological function of cells, binds biomolecules such as growth factors, and maintains extracellular homeostasis. Abnormalities in the ECM are implicated in a variety of diseases, such as osteogenesis imperfecta, Marfan's syndrome, and other genetic disorders.[2] Changes in the ECM can also lead to more common disorders such as coronary heart disease, in which the ECM continually binds and accumulates lipoproteins, contributing to the build-up of atherosclerotic plaque.[3] Thus, preventing or treating ECM-related diseases involves studying and understanding the ECM.

The major components of the ECM are water, proteins, and polysaccharides.[1] Proteoglycans and fibrous proteins, such as collagens, elastins, and fibronectins, are the two main types of macromolecules in the ECM. Proteoglycans make up most of the ECM, forming a hydrated gel that acts as a mechanical buffer, maintains structural integrity, and provides binding points for cells or ligands. The most abundant fibrous proteins are the collagens, which are secreted by fibroblasts, contributing up to 30% of the total protein by mass of a multicellular organism.[1,4] Collagen networks provide tensile strength, support cell adhesion and migration, and play a role in the development of tissues.[1] Although there are more than 20 identified types of collagen, usually one type

dominates in any given tissue (e.g., Type I collagen in bone and ligaments).[5] Collagen associates with another major ECM fibrous protein, elastin, which allows tissues to be stretched repeatedly.[1] The elasticity of tissues such as the lungs, dermis, and blood vessels is provided by the elastin fibers in the ECM.[6] The elasticity of the ECM also plays a role in stem cell differentiation.[7] Fibronectin, another major fibrous protein, directs interstitial ECM organization and mediates cell attachment and migration.[1] Furthermore, networks of proteoglycans and glycosaminoglycans help the ECM withstand tensile and compressive stresses.[8] The ECM is highly dynamic and constantly remodels in order to appropriately respond to stress and wound healing. *In vivo*, epithelial tissue homeostasis is regulated by interactions with the surrounding adipocytes and fibroblasts, which secrete and organize type I and III collagens, elastin, fibronectins, and proteoglycans to maintain the integrity of the ECM.[9] The composition and topography of the ECM is unique and dependent on the type and state of the developing tissue, which is important to consider when developing *in vitro* mimics of the ECM.[1]

In addition to genetic abnormalities in ECM proteins leading to a wide range of syndromes, the ECM also plays a crucial role in the development of tumours,[10] which has been associated with defects in the normal wound repair process.[11] Tumours are stiffer than healthy tissue due to increased ECM deposition,[10] and the increased presence of chemokines and growth factors, such as vascular endothelial growth factor (vEGF), increases vascular permeability and tumor growth.[12] These events contribute to a positive feedback loop that ultimately induces angiogenesis and metastasis.[13] For example, increased deposition and crosslinking of collagen I contributes to stiffer tissue, and is

linked to an increased incidence of breast cancer and metastasis.[14] Targeting ECM components, such as by disrupting collagen I crosslinking, has shown to be successful in inhibiting metastasis in pre-clinical models and remains a promising method to disrupt cancer progression.[14] Overall, the importance of the ECM in the development of many diseases has prompted the study of its properties to understand the mechanisms by which it directs cellular behaviour.

1.2 Current approaches to mimic the ECM

1.2.1 Natural ECMs

The ECM has been imitated through a variety of approaches to better understand how its fundamental biochemical/physical properties govern the molecular mechanisms of cell behaviour.[1] For example, Matrigel™, a reconstituted basement membrane derived from mouse carcinoma, has the ability to retain stem cells in an undifferentiated state and is commonly used to study cell differentiation, angiogenesis, and tumour growth.[15,16] Although this gel can mimic some properties of epithelial basement membranes, it has several disadvantages.[1] First, since Matrigel™ is derived from mouse tumor cells, its composition is not well-defined, which can lead to variability in experimental results.[15] Furthermore, it fails to mimic the physical state of the 3D native ECM in tissues.[1] Other natural scaffolds that have been developed include fibrin or type I collagen.[17,4] Fibrin has been used in biodegradable scaffolds; however, these scaffolds lack mechanical strength and structural integrity compared to the native ECM.[17,1] Since collagen is the most abundant protein in the ECM, scaffolds comprised of Type I collagen have also been explored and can assemble into fibrils that can be oriented, functionalized, or

crosslinked.[4] Type I collagen scaffolds can mimic some of the biological aspects of the ECM and be used to further study the effects of collagen stiffness on tumor growth and metastasis.[4] However, collagen scaffolds have high levels of heterogeneity, which can greatly impact their pore sizes and organization.[18,1] While natural ECM mimics recapitulate some of the physical and biological properties of the native ECM, they are often difficult to chemically and physically define.

To understand the molecular and biophysical mechanisms which prompt specific cellular behavior, such as morphogenesis and differentiation, it is necessary to develop scaffolds that are well-defined and reproducible. In addition, the chemical or physical properties of well-defined scaffolds with specific reactive groups can potentially be fine-tuned by post-functionalization to probe cell behaviour.[19] Post-functionalization can be useful since proteins, such as fibronectin and vitronectin, can adsorb onto scaffolds and mediate focal adhesions that allow cells to attach onto the material.[20] The type, quantity, and conformation of proteins adsorbed onto a material greatly depend on its surface charge and wettability. For example, moderately hydrophilic surfaces or positively charged surface functional groups generally promote the highest levels of fibroblast attachment.[20] Similarly, peptides containing the cell recognition motif RGD (arginine, glycine, aspartic acid) have been used to modify a wide range of polymers in biomaterials to promote cell attachment or study the role of the motif in cell adhesion.[21] Thus, the ability to fine tune the chemical and physical properties of biomimetic scaffolds through post-functionalization is important in manipulating and understanding their effects on cellular behaviour.

1.2.2 Synthetic ECMs

Synthetic polymer scaffolds with well-defined chemical and physical properties are being increasingly explored to address the issue of reproducibility and tunability.[19] For example, hydrogels of acrylated polyethylene glycol grafted with cell adhesive peptides are chemically and physically well-defined and are able to support cell adhesion and growth.[19] Synthetic polymer hydrogels can be functionalized chemically or by enzymatic reactions to tune their surface chemistry and better mimic the physiochemical properties of the ECM.[22] However, 2D polymer scaffolds fail to exhibit the organization and physical motifs that mimic natural collagen networks in the ECM.[1] To better mimic these structural features, peptide-based nanofiber scaffolds, which can form secondary structures and mimic the collagen triple helix of the ECM, have been studied.[23] Peptide scaffolds have the additional advantage that they can be covalently modified to mimic native proteins and have been shown to support stem cell growth. Overall, the most recent developments in the field of ECM mimics involve scaffolds whose properties can be strictly controlled, including their fiber or structure size, stiffness, orientation, and surface chemistry, providing new methods to explore and understand the ECM.[1,19]

1.3 Electrospinning and applications

Electrospinning is a technique that can be used to produce polymer fibers with diameters ranging from 3 nm to greater than 5 μm.[24] Nanofibrous polymer scaffolds have been of interest for their potential applications in filtration membranes, fibrous sensors,

and tissue engineering.[25,26,27] The set up for electrospinning is simple and inexpensive, consisting mainly of a conductive tip, a high voltage source, and a grounded collector (Figure 1.1).[24] The presence of an electric field from the high-voltage source ionizes the polymer solution at the tip of the syringe. The electrostatic repulsion within the solution and the electrostatic attraction to the collector are opposed by the surface tension of the droplet at the needle tip. Once the electrostatic forces overcome this surface tension, a polymer jet is extracted. As the polymer jet travels towards the collector, the solvent evaporates and electric forces continue to stretch the jet, decreasing the diameter of the polymer fiber down to the micro- to nanometer range as it deposits onto the collector. Important parameters of electrospinning include the solution properties, such as viscosity, surface tension, conductivity, entanglement concentration of the polymer, and the dielectric constant of the solvent. Controlled variables include the flow rate of the syringe pump, distance between needle tip-to-collector, strength of the electric field, temperature, and humidity. Overall, the electrospinning process and the morphologies of the resultant polymer fibers can be controlled by using a variety of parameters.

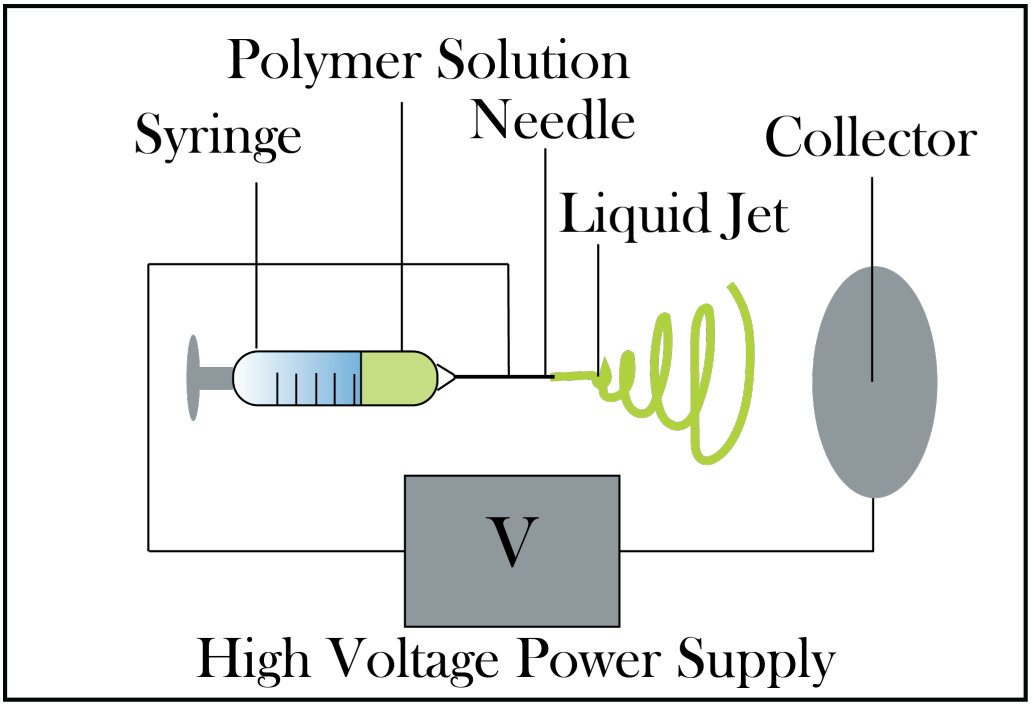

Figure 1.1. Simplified electrospinning set-up consisting of a syringe usually driven by a motorized pump (not shown), a high voltage source, and a rotating or static collector.

Polymer nanofibrous scaffolds with high surface-to-volume ratios and good permeability for nutrient exchange can be used as tissue engineering scaffolds, providing a 3D ECM-mimetic framework for cells to attach and grow *in vitro* prior to implantation into the body.[24] Both synthetic and natural polymer nanofibers have been explored for cellular scaffold applications. For example, synthetic electrospun poly(lactic-*co*-glycolic acid) (PLGA) scaffolds exhibit high surface areas and porosities, which facilitate the formation of focal adhesions and cell attachment.[27] Natural electrospun polymeric scaffolds, such as collagen nanofibers, can also mimic the chemical and biological aspects of the native ECM.[28] Furthermore, natural polymers including collagen, alginate, and starch, can be incorporated into synthetic nanofibrous scaffolds to increase cell and tissue compatibility.[29,30] A variety of electrospun nanofibrous scaffolds have been able to

support different cell types, including mouse fibroblasts on PLGA nanofibers,[27] fetal bovine chondrocytes on poly(ε-caprolactone) (PCL) nanofibers,[31] and rat kidney cells on polyamide nanofibers.[32] Additionally, Venugopal *et al.* (2005) coated electrospun collagen with PCL, creating scaffolds that can mimic the skin and support the attachment and growth of human dermal fibroblasts.[33] Huang *et al.* (2000) electrospun a synthetic peptide sequence of elastin, a major component of the ECM that provides tissues with elasticity, resulting in nanofiber scaffolds with a Young's modulus of 1.8 GPa to mimic the mechanical properties of blood vessels.[34] However, one disadvantage to using biological materials is reduced versatility as there are limited solvents that can maintain the integrity of the materials during electrospinning.[35] In this thesis, a synthetic polyampholyte was used to fabricate electrospun nanofibers to be used as tunable, biomimetic cellular scaffolds.

1.4 Microstructured films and applications

Another method to fabricate 3D scaffolds to mimic the ECM involves creating microstructured surfaces. This thesis focusses primarily on microstructured films prepared through wrinkling during the thermal shrinking of pre-stressed polystyrene (PS) supports coated with a bio-relevant polyampholyte.[36,37] PS is a widely used, commercially available shape-memory thermoplastic polymer.[36] Two-dimensional stretching of PS near its glass transition temperature (T_g) followed by immediate cooling leads to sheets containing polymer chains frozen in a stretched, two-dimensionally aligned state. Subsequent heating of these sheets above the T_g leads to rapid relaxation of the stretched

chains into their random coil conformations, which causes substantial 2-dimensional macroscopic shrinking of the PS film (Figure 1.2).[38] Thus, heating pre-stressed PS above its T_g (90°C), but below its melting temperature (240°C), shrinks the film down to 16% of its pre-heated area as a result of polymer chain relaxation.[36,39]

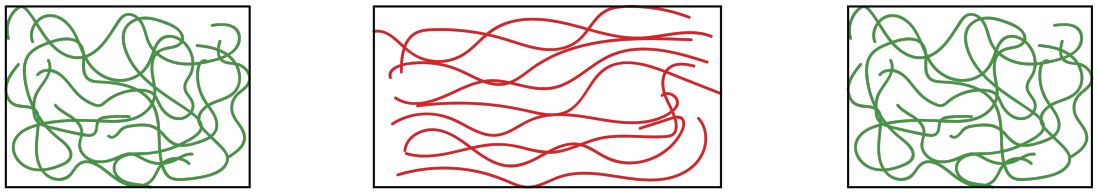

Figure 1.2. Thermoplastic polymer programming.[38] In their relaxed state, polymer chains adopt the entropically favoured, random three-dimensional coil conformation. Heating above the T_g followed by stretching in one dimension (shown here) or two dimensions leads to preferential alignment of the individual polymer chains along the stretching direction(s), an entropically less stable conformation which can be frozen by rapid cooling below T_g. When the polymer is subsequently heated above its T_g, the polymer chains return to their original configuration in the entropically favored state, causing one or two-dimensional film shrinkage.

If the PS substrates are coated with another polymer, shrinking the PS substrates by heating above 90°C introduces compressive stress that can wrinkle and buckle films printed or deposited on top of the thermoplastic substrate, which results in micro/nanostructured films (Figure 1.3a).[36] Provided the elastic modulus of the deposited film is different from the PS substrate (2-3 GPa at room temperature), the compression from the shrinking causes buckling instability to occur on the film's surface to release strain, resulting in wrinkles with a defined wavelength (λ) and amplitude (A) (Figure 1.3b).[40] For a substrate that shrinks biaxially, the interference of wrinkles in perpendicular

directions results in less order and more random wrinkling.[39] The wrinkle wavelength of the structures can be adjusted by changing the thickness of the deposited film, as the wavelength is proportional to the film thickness. The wavelength of biaxial wrinkling depends on the Poisson ratios, elastic moduli of the film and substrate (ν_f, E_f and ν_s, E_s, respectively), and the thickness of the film (h) (Equation 1).[37]

$$\lambda = 2\pi h \left[\frac{(1-{\nu_s}^2)E_f}{3(1-{\nu_f}^2)E_s}\right]^{1/3} \quad (Equation\ 1)$$

Another parameter of surface wrinkling is the critical strain (ε_c) required to produce wrinkling in the system, which only depends on the modulus ratio of the substrate and the film.[40] Once the applied strain (ε) exceeds the critical strain (ε_c), the additional strain is released by the increase in the wrinkling amplitude (A), while λ stays constant (Equation 2).

$$A = h\sqrt{\frac{\varepsilon - \varepsilon_c}{\varepsilon_c}} \quad (Equation\ 2)$$

The wavelength of the instability, the critical strain, and the amplitude growth as a function of strain, are the three key parameters that describe the mechanisms of surface wrinkling.[40] This simple and inexpensive bench-top technique has been previously used to fabricate micro/nanostructured surfaces out of a variety of thin films, as well as to calculate the elastic moduli of nanobiocomposite films.[36,41-44]

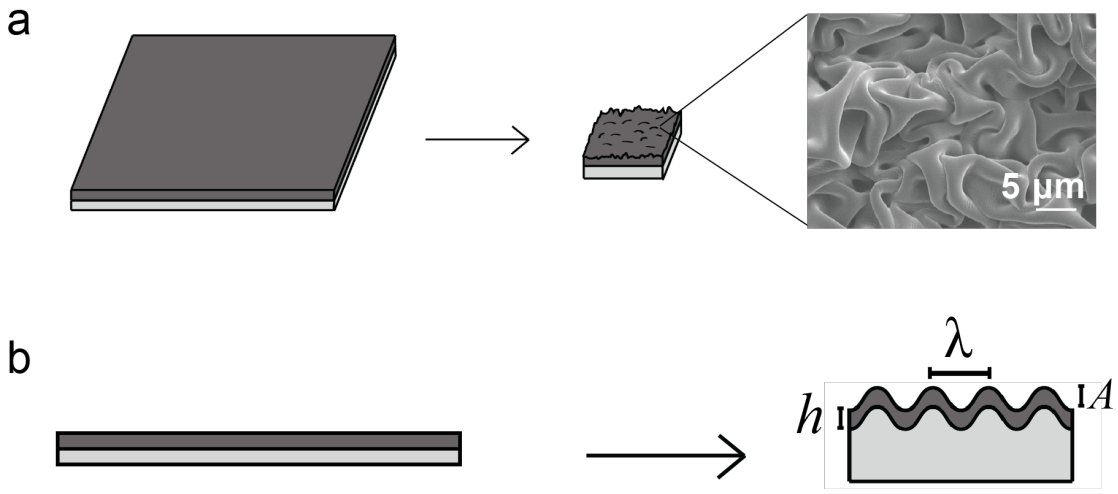

Figure 1.3. Fabrication of microstructured films. a) Heating the pre-stressed polystyrene above its glass transition temperature of 90°C shrinks the film down to 16% of its original size. The deposited film on top of the polystyrene wrinkles and buckles, creating microstructured thin films. **b)** Uniaxial shrinking causes a defined wavelength (λ) given a constant film thickness (h). For a substrate that shrinks biaxially, the interference of wrinkles in perpendicular directions results in less order and more random wrinkling.[39]

Microstructured films can provide high surface areas and 3D environments to be used as ECM mimics for cellular scaffolds. Cellular behaviour on nano/microstructured surfaces has been explored in tissue engineering and regenerative medicine due to the importance of understanding the mechanisms of cell response to the biophysical environment.[45] Cellular behaviour is governed through both intrinsic and extrinsic cell signals. Extrinsic signals, such as cell to cell or cell to ECM contact can be chemical (e.g. growth factors), or mechanical (e.g. tensile forces from micro/nanostructured surfaces). The strength of integrin-cytoskeleton connections can depend on mechanical stress, indicating the role of mechanical signals in activating certain intracellular pathways.[45] Additionally, adherent cells can respond to the topography of their environment by orienting along substrate patterns though contact guidance, first observed in embryonic

cells by Harrison *et al*.[46] Since then, there have been many reports in the literature of cells conforming or aligning to micro/nanostructured surfaces.[47,48,49,50] For example, human gingival fibroblasts conformed and aligned along the groove axes in microstructured silicon dioxide surfaces.[49] Furthermore, Jiang *et al*. observed bovine capillary endothelial cells elongating and spreading along the structures of fibronectin-coated wrinkled surfaces, as the scaffolds provided cells with contact guidance.[50] In addition, micropatterned substrates of varying structures can alter endothelial cell spreading, leading to growth, apoptosis or differentiation, depending on the geometry of cell spreading.[51-53] An advantage to studying cells on microstructured surfaces include the higher relevance to *in vivo* settings, as microstructures provide 3D environments that mimic the ECM. Compared to fibroblasts seeded onto flat polydimethylsiloxane (PDMS) surfaces, fibroblasts seeded onto microstructured PDMS scaffolds demonstrated lower cytoskeletal stress, similar to fibroblasts *in vivo*.[48] Overall, microstructured films can be used as relevant ECM mimics to study cell attachment, migration, and differentiation. In this thesis, a synthetic polyampholyte was used to fabricate microstructured films to be used as tunable, 3D scaffolds to study fibroblast response to different topographies and surface chemistries.

1.5 Polyampholytes and their biomedical applications

Polyampholytes are polymers that possess both cationic and anionic units and have received much attention in biomedical applications in the past decade due to their unique abilities to respond to pH, ionic strength, and temperature.[54] In addition,

polyampholytes can mimic the chemical properties of polypeptides and proteins, which mediate many important biological functions in an organism. Polyampholytes can be synthesized through free radical co-polymerization of the cationic and anionic monomers, and can be composed of different combinations of weak or strong cationic and anionic units.[54,55] This classification is important because the weaker the functional group is, the greater the functional unit responds to pH changes, changing the swelling behaviour of the entire polymer in aqueous solution.[55] At the isoelectric point, the degree of swelling is lower than at higher or lower pH levels; since charges are balanced, electrostatic interactions between the anionic and cationic units cause the polymer to collapse. In contrast, at lower or higher pH, electrostatic repulsion between the charged units causes the polymer to expand. Furthermore, the concentration of salt can also influence the swelling behaviour of polyampholytes. At high salt concentrations, the electrostatic interactions between the oppositely charged units are shielded, which causes the size and viscosity of the polymer in solution to increase, which is termed as the antipolyelectrolyte effect. Overall, the behaviour of polyampholytes can be controlled by composition, pH, ionic strength, and temperature, allowing them to be used in a variety of applications.

The unique abilities of polyampholytes to respond to pH, ionic strength, and temperature allow them to be applied in many biological applications, including in drug delivery, separation, sensors, and biomimetic materials.[55-58] Due to the pH and temperature-responsive properties of polyampholytes, the adsorption and release of biomolecules can be controlled using these parameters. For example, controlled albumin adsorption (maximal at high pH) and release (at low pH) from a 2-methylimidazole and

ethylene glycol diglycidyl polyampholyte has been demonstrated through manipulation of the electrostatic interactions.[59] Others have used polyampholytes to coat surfaces to prevent biofouling in materials used in applications for tissue engineering.[60] The pH-responsive properties of polyampholytes have also led to the development of polymer brushes that act as bacterial catch-and-release surfaces.[61] Under acidic conditions, the cationic polymer brushes promote the adhesion of bacteria, while under neutral or basic conditions, the polymer brush is non-fouling and prevents bacterial adhesion. To further take advantage of the pH and temperature-sensitive properties, microgel polyampholyte systems that are able to load and release small molecules have been developed for drug delivery applications.[55,56] In addition, polyampholytes are generally biocompatible, which makes them good candidates for the development of hydrogel scaffolds for tissue engineering applications.[58] Certain polyampholyte scaffolds are resistant to non-specific protein adsorption, which improves the wound healing response and prevents the foreign body response from attacking the biomaterial. Overall, the unique pH and temperature responsive properties and tunability of polyampholytes, makes them attractive materials for a wide range of applications, including drug delivery, sensors, or biomimetic materials. The work presented in this thesis revolves around a synthetic polyampholyte used to fabricate microstructured films and electrospun nanofibers, which were subsequently used as chemically tunable and biocompatible surfaces for cell studies.

1.6 p(APM-*co*-AA) – a polyampholyte for the fabrication of cellular scaffolds

A random co-polyampholyte system consisting of N-(3-aminopropyl)methacrylamide hydrochloride and acrylic acid [p(APM-*co*-AA)] has been

well-characterized by the Stöver group (Scheme 1.1).[62] p(APM-*co*-AA) can be net cationic or anionic depending on co-monomer ratio and pH, as the APM units are positively charged below a pH of ~9.1 and the AA units are negatively charged above a pH of ~4.3, or net neutral at its predicted pI of ~7.5 for the 1:1 copolymer. The behaviour of this polyampholyte system can be controlled by composition, pH, ionic strength, and temperature, making it a good candidate in creating tunable scaffolds.

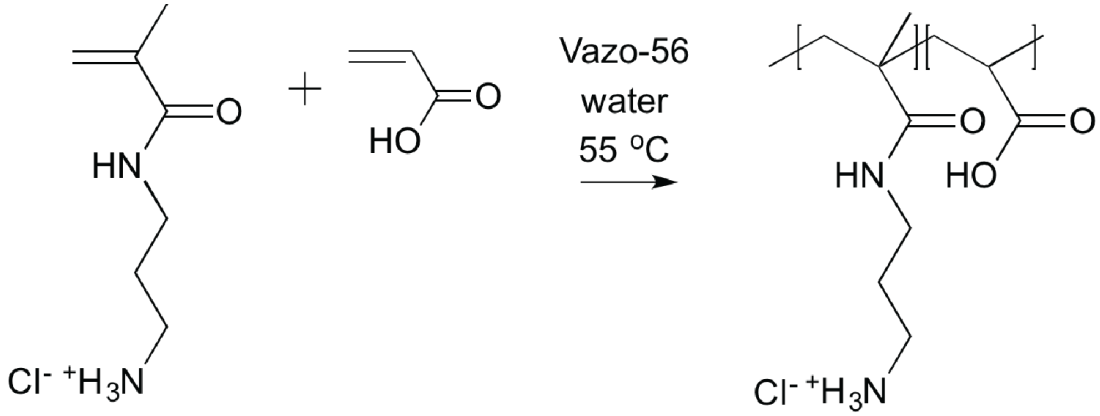

Scheme 1.1. Free radical co-polymerization of APM and AA monomers to form p(APM-*co*-AA). p(APM-*co*-AA) can be prepared by free radical batch-copolymerization.[62]

Previous work in our group has shown that heating anhydrous p(APM-*co*-AA) led to crosslinked polymers that were swellable but did not dissolve at any pH [Jing Zhao, private communication]. An analogous reaction has been studied for layer-by-layer films formed from poly(allyl amine) and poly(acrylic acid), where drying leads to anhydride formation, followed by formation of amide crosslinks.[63] This is the first report of heating p(APM_{10}-*co*-AA_{90}) in anhydrous conditions leading to anhydride formation and subsequent intra- and inter-molecular crosslinking through amide formation. This crosslinking mechanism involves adjacent acrylic acid units dehydrating to form

anhydrides (Scheme 1.2). Then, the amine from an APM unit in a neighbouring polymer chain reacts with the anhydride, providing intermolecular crosslinking. Such crosslinking without the use of added small molecule cross-linkers such as glutaraldehyde can increase the structural integrity of materials without introducing potentially cytotoxic small molecules. In addition, residual anhydride groups available after heating allow chemical modification using nucleophilic groups, such as amines. Using simple chemistry to manipulate biological behaviour provides cheaper and controllable methods to produce materials for studying cell behaviour or scaffolds for tissue engineering. The ability to fine tune the composition, surface chemistry, and wettability of the p(APM-*co*-AA) system makes it an ideal candidate for fabricating biomimetic scaffolds.

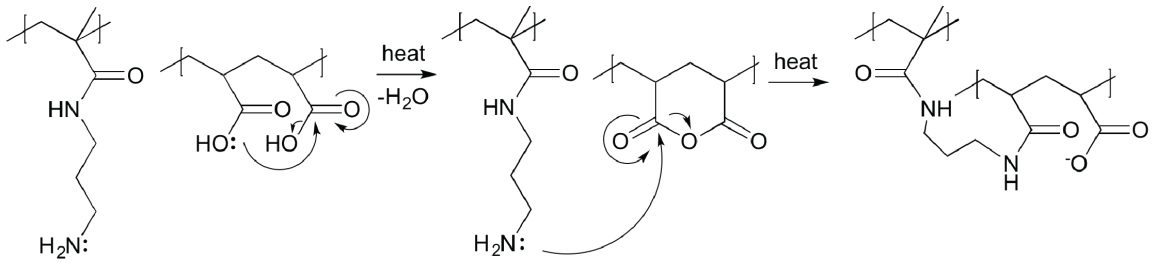

Scheme 1.2. p(APM-*co*-AA) crosslinks with itself under heat and anhydrous conditions. The proposed mechanism of crosslinking occurs when adjacent acrylic acid units dehydrate to form anhydride moieties. The amine from the APM unit then attacks the anhydride to form intermolecular crosslinks.

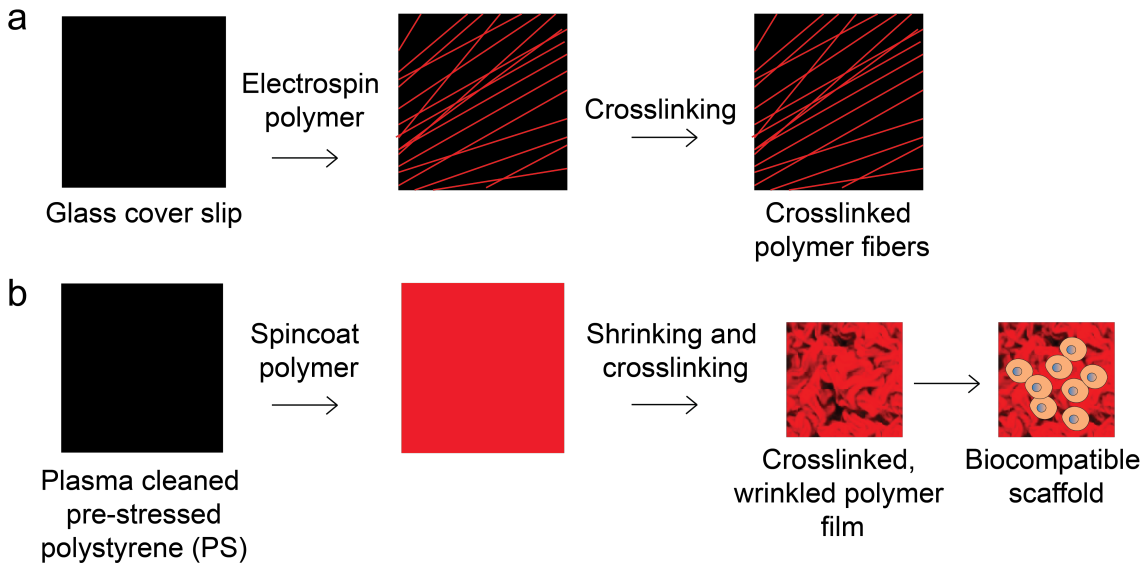

Scheme 1.3. Fabrication of nanofibrous scaffolds and microstructured thin films from p(APM-*co*-AA). a) Nanofibrous scaffolds were fabricated using electrospinning and **b)** microstructured thin films were fabricated on PS and then shrunken and crosslinked under heat. NIH 3T3 murine fibroblasts were then seeded onto the scaffolds to investigate cell behaviour as a response to different film surface chemistries and topographies.

This thesis explores the fabrication of microstructured and nanofibrous scaffolds made from p(APM-*co*-AA) and the effects of scaffold surface chemistry and topography on fibroblast behaviour (Scheme 1.3). Chapter 2 presents for the first time, the use of a shape-memory polymer structuring approach to fabricate scaffolds with tunable properties from a polyampholyte thin film. The crosslinking of the materials and structural integrity of the crosslinked scaffolds are confirmed and described. Furthermore, the surface chemistry and topography tunability of these scaffolds are demonstrated and characterized. The effects of surface chemistry and topography on fibroblast morphology were studied under fluorescence microscopy using these tunable properties of the microstructured films. Chapter 3 presents the use of electrospinning for the formation of

nanofibrous mats from a synthetic polyampholyte for the first time. The challenges associated with finding the optimal conditions for electrospinning are discussed and suitable conditions to form fibers from p(APM-*co*-AA) are presented. The crosslinked scaffolds were characterized and cell attachment onto the scaffolds were also explored. Chapter 4 outlines the advantages and conclusions of this polyampholyte system, in addition to suggesting future work and extensions of this project. Overall, our self-crosslinking p(APM-*co*-AA) scaffolds can be used in a variety of applications and the system's chemical and topographical tunability makes it a great candidate for probing specific cellular responses, providing a new tool to study and understand the ECM and its properties.

1.7 References

(1) Frantz, C., Stewart, K. M., and Weaver, V. M. (2010) The extracellular matrix at a glance. *J. Cell Sci. 123*, 4195–4200.

(2) Jarvelainen, H., Sainio, A., Koulu, M., Wight, T. N., and Penttinen, R. (2009) Extracellular matrix molecules: potential targets in pharmacotherapy. *Pharmacol. Rev. 61*, 198–223.

(3) Williams, K. J., and Tabas, I. (1995) The response-to-retention hypothesis of early atherogenesis. *Arterioscler. Thromb. Vasc. Biol. 15*, 551–561.

(4) Friess, W. (1998) Collagen – biomaterial for drug delivery. *Eur. J. Pharm. Biopharm. 45*, 113–136.

(5) Gelse, K. (2003) Collagens—structure, function, and biosynthesis. *Adv. Drug Delivery Rev. 55*, 1531–1546.

(6) Rosenbloom, J., Abrams, W. R., and Mecham, R. (1993) Extracellular matrix 4: the elastic fiber. *FASEB J 7*, 1208–1218.

(7) Engler, A. J., Sweeney, H. L., and Discher, D. E. (2007) Extracellular matrix elasticity directs stem cell differentiation. *J. Musculoskelet. Neuronal Interact. 7*, 335.

(8) Scott, J. E. (2003) Elasticity in extracellular matrix "shape modules" of tendon, cartilage, etc. A sliding proteoglycan-filament model. *J. Physiol. 553*, 335–343.

(9) Ronnov-Jessen, L., Petersen, O. W., and Bissell, M. J. (1996) Cellular changes involved in conversion of normal to malignant breast: importance of the stromal reaction. *Phys. Rev. 76*, 69–125.

(10) Cox, T. R., and Erler, J. T. (2011) Remodeling and homeostasis of the extracellular matrix: implications for fibrotic diseases and cancer. *Dis. Model. Mech. 4*, 165–178.

(11) Schäfer, M., and Werner, S. (2008) Cancer as an overhealing wound: an old hypothesis revisited. *Nat. Rev. Mol. Cell Biol. 9*, 628–638.

(12) Bosman, F. T., and Stamenkovic, I. (2003) Functional structure and composition of the extracellular matrix. *J. Pathol.* (Bosman, F. T., and Stamenkovic, I., Eds.) *200*, 423–428.

(13) Butcher, D. T., Alliston, T., and Weaver, V. M. (2009) A tense situation: forcing tumour progression. *Nat. Rev. Cancer 9*, 108–122.

(14) Venning, F. A., Wullkopf, L., and Erler, J. T. (2015) Targeting ECM disrupts cancer progression. *Frontiers in Oncology 5*, 1377.

(15) Hughes, C. S., Postovit, L. M., and Lajoie, G. A. (2010) Matrigel: A complex protein mixture required for optimal growth of cell culture. *Proteomics 10*, 1886–1890.

(16) Kleinman, H. K., and Martin, G. R. (2005) Matrigel: Basement membrane matrix with biological activity. *Semin. Cancer Biol. 15*, 378–386.

(17) Blombäck, B., and Bark, N. (2004) Fibrinopeptides and fibrin gel structure. *Biophys. Chem. 112*, 147–151.

(18) Johnson, K. R., Leight, J. L., and Weaver, V. M. (2007) Demystifying the effects of a three-dimensional microenvironment in tissue morphogenesis, in *Cell Mechanics*, pp 547–583. Elsevier.

(19) Lutolf, M. P., and Hubbell, J. A. (2005) Synthetic biomaterials as instructive extracellular microenvironments for morphogenesis in tissue engineering. *Nature Biotechnol. 23*, 47–55.

(20) Webb, K., Hlady, V., and Tresco, P. A. (1998) Relative importance of surface wettability and charged functional groups on NIH 3T3 fibroblast attachment, spreading, and cytoskeletal organization. *J. Biomed. Mater. Res. 41*, 422–430.

(21) Hersel, U., Dahmen, C., and Kessler, H. (2003) RGD modified polymers: biomaterials for stimulated cell adhesion and beyond. *Biomaterials 24*, 4385–4415.

(22) Ehrbar, M., Rizzi, S. C., Schoenmakers, R. G., San Miguel, B., Hubbell, J. A., Weber, F. E., and Lutolf, M. P. (2007) Biomolecular hydrogels formed and degraded via site-specific enzymatic reactions. *Biomacromolecules 8*, 3000–3007.

(23) Hauser, C. A. E., and Zhang, S. (2010) Designer self-assembling peptide nanofiber biological materials. *Chem. Soc. Rev. 39*, 2780–2790.

(24) Pham, Q. P., Sharma, U., and Mikos, D. A. G. (2006) Electrospinning of polymeric nanofibers for tissue engineering applications: a review. *J. Tissue Eng. 12*, 1197–1211.

(25) Gopal, R., Kaur, S., Ma, Z., Chan, C., Ramakrishna, S., and Matsuura, T. (2006) Electrospun nanofibrous filtration membrane. *J. Membr. Sci. 281*, 581–586.

(26) Wang, J., Zou, B., Ruan, S., Zhao, J., Chen, Q., and Wu, F. (2009) HCHO sensing properties of Ag-doped In_2O_3 nanofibers synthesized by electrospinning. *Mater. Lett. 63*, 1750–1753.

(27) Li, W. J., Laurencin, C. T., Caterson, E. J., Tuan, R. S., and Ko, F. K. (2002) Electrospun nanofibrous structure: A novel scaffold for tissue engineering. *J. Biomed. Mater. Res. 60*, 613–621.

(28) Matthews, J. A., Wnek, G. E., Simpson, D. G., and Bowlin, G. L. (2002) Electrospinning of collagen nanofibers. *Biomacromolecules 3*, 232–238.

(29) Wayne, J. S., McDowell, C. L., Shields, K. J., and Tuan, R. S. (2005) *In vivo* response of polylactic acid–alginate scaffolds and bone marrow-derived cells for cartilage tissue engineering. *J. Tissue Eng. 11*, 953–963.

(30) Pavlov, M. P., Mano, J. F., Neves, N. M., and Reis, R. L. (2004) Fibers and 3D Mesh Scaffolds from Biodegradable Starch-Based Blends: Production and Characterization. *Macromol. Biosci. 4*, 776–784.

(31) Li, W. J., Danielson, K. G., Alexander, P. G., and Tuan, R. S. (2003) Biological response of chondrocytes cultured in three-dimensional nanofibrous poly(ϵ-caprolactone) scaffolds. *J. Biomed. Mater. Res. 67A*, 1105–1114.

(32) Schindler, M., Ahmed, I., Kamal, J., Nur-E-Kamal, A., Grafe, T. H., Young Chung, H., and Meiners, S. (2005) A synthetic nanofibrillar matrix promotes *in vivo*-like organization and morphogenesis for cells in culture. *Biomaterials 26*, 5624–5631.

(33) Venugopal, J., and Ramakrishna, S. (2005) Biocompatible nanofiber matrices for the engineering of a dermal substitute for skin regeneration. *J. Tissue Eng. 11*, 847–854.

(34) Huang, L., McMillan, R. A., Apkarian, R. P., Pourdeyhimi, B., Conticello, V. P., and Chaikof, E. L. (2000) Generation of synthetic elastin-mimetic small diameter fibers and fiber networks. *Macromolecules 33*, 2989–2997.

(35) Zhang, Y., Ouyang, H., Lim, C. T., Ramakrishna, S., and Huang, Z. M. (2005) Electrospinning of gelatin fibers and gelatin/PCL composite fibrous scaffolds. *J. Biomed. Mater. Res. 72B*, 156–165.

(36) Gabardo, C. M., Zhu, Y., Soleymani, L., and Moran-Mirabal, J. M. (2013) Bench-top fabrication of hierarchically structured high-surface-area electrodes. *Adv. Funct. Mater. 23*, 3030–3039.

(37) Genzer, J., and Groenewold, J. (2006) Soft matter with hard skin: From skin wrinkles to templating and material characterization. *Soft Matter 2*, 310–14.

(38) Lendlein, A., and Kelch, S. (2002) Shape-memory polymers. *Angew. Chem. Int. Ed. Engl. 41*, 2034–2057.

(39) Gabardo, C. M., Hosseini, A., and Soleymani, L. (2017) A new wrinkle in biosensors: wrinkled electrodes could be a breakthrough for lab-on-a-chip devices. *IEEE Nanotechnol. Mag. 10*, 6–18.

(40) Chung, J. Y., Nolte, A. J., and Stafford, C. M. (2010) Surface wrinkling: a versatile

platform for measuring thin-film properties. *Adv. Mater. 23*, 349–368.

(41) Zhu, Y., and Moran-Mirabal, J. (2016) Highly bendable and stretchable electrodes based on micro/nanostructured gold films for flexible sensors and electronics. *Adv. Electron. Mater. 2*, 1500345.

(42) Gill, U., Sutherland, T., Himbert, S., Zhu, Y., Rheinstädter, M. C., Cranston, E. D., and Moran-Mirabal, J. M. (2017) Beyond buckling: humidity-independent measurement of the mechanical properties of green nanobiocomposite films. *Nanoscale 9*, 7781–7790.

(43) Sonney, S., Shek, N., and Moran-Mirabal, J. M. (2015) Rapid bench-top fabrication of poly(dimethylsiloxane)/polystyrene microfluidic devices incorporating high-surface-area sensing electrodes. *Biomicrofluidics 9*, 026501.

(44) Gratton, E., Sharma, H., Khine, M., Digman, M. A., and Felsinger, N. (2014) Enhanced emission of fluorophores on shrink-induced wrinkled composite structures. *Opt. Mater. Express, OME 4*, 753–763.

(45) Martínez, E., Engel, E., Planell, J. A., and Samitier, J. (2009) Effects of artificial micro- and nano-structured surfaces on cell behaviour. *Ann. Anat. 191*, 126–135.

(46) Harrison, R. G. (1911) On the stereotropism of embryonic cells. *Science 34*, 279–281.

(47) Kim, D.-H., Provenzano, P. P., Smith, C. L., and Levchenko, A. (2012) Matrix nanotopography as a regulator of cell function. *J. Cell Biol. 197*, 351–360.

(48) Stanton, M. M., Parrillo, A., Thomas, G. M., McGimpsey, W. G., Wen, Q., Bellin, R. M., and Lambert, C. R. (2014) Fibroblast extracellular matrix and adhesion on microtextured polydimethylsiloxane scaffolds. *J. Biomed. Mater. Res. 103*, 861–869.

(49) Meyle, J., Wolburg, H., and Recum, Von, A. F. (1993) Surface micromorphology and cellular interactions. *J. Biomater. Appl. 7*, 362–374.

(50) Jiang, X., Takayama, S., Qian, X., Ostuni, E., Wu, H., Bowden, N., LeDuc, P., Ingber, D. E., and Whitesides, G. M. (2002) Controlling mammalian cell spreading and cytoskeletal arrangement with conveniently fabricated continuous wavy features on poly(dimethylsiloxane). *Langmuir 18*, 3273–3280.

(51) Chen, C. S., Mrksich, M., Huang, S., Whitesides, G. M., and Ingber, D. E. (1997) Geometric control of cell life and death. *Science 276*, 1425–1428.

(52) Mrksich, M. (2000) A surface chemistry approach to studying cell adhesion. *Chem. Soc. Rev. 29*, 267–273.

(53) Dike, L. E., Chen, C. S., Mrksich, M., Tien, J., Whitesides, G. M., and Ingber, D. E.

(1999) Geometric control of switching between growth, apoptosis, and differentiation during angiogenesis using micropatterned substrates. *In Vitro Cell. Dev. Biol.-Anim. 35*, 441–448.

(54) Singh, P. K., Singh, M., and Singh, V. K. (2007) Zwitterionic Polyelectrolytes: A Review : e-Polymers. *e-polymers* 1618–7229.

(55) Zurick, K. M., and Bernards, M. (2013) Recent biomedical advances with polyampholyte polymers. *J. Appl. Polym. Sci. 131*, 10.1002–app.40069.

(56) Yoshihara, C., Shew, C.-Y., Ito, T., and Koyama, Y. (2010) Loosening of DNA/polycation complexes by synthetic polyampholyte to improve the transcription efficiency: effect of charge balance in the polyampholyte. *Biophys. J. 98*, 1257–1266.

(57) Chakrabarty, T., and Shahi, V. K. (2013) (3-glycidoxypropyl) Trimethoxy silane induced switchable zwitterionic membrane with high protein capture and separation properties. *J. Membr. Sci. 444*, 77–86.

(58) Schroeder, M. E., Zurick, K. M., McGrath, D. E., and Bernards, M. T. (2013) Multifunctional polyampholyte hydrogels with fouling resistance and protein conjugation capacity. *Biomacromolecules 14*, 3112–3122.

(59) Leal Denis, M. F., Carballo, R. R., Spiaggi, A. J., Dabas, P. C., Campo Dall' Orto, V., Martínez, J. M. L., and Buldain, G. Y. (2008) Synthesis and sorption properties of a polyampholyte. *React. Funct. Polym. 68*, 169–181.

(60) Utrata-Wesolek, A. (2013) Antifouling surfaces in medical application. *Polimery-W 58*, 685–695.

(61) Mi, L., Bernards, M. T., Cheng, G., Yu, Q., and Jiang, S. (2010) pH responsive properties of non-fouling mixed-charge polymer brushes based on quaternary amine and carboxylic acid monomers. *Biomaterials 31*, 2919–2925.

(62) Zhao, J., Burke, N. A. D., and Stöver, H. D. H. (2016) Preparation and study of multi-responsive polyampholyte copolymers of N -(3-aminopropyl)methacrylamide hydrochloride and acrylic acid. *RSC Adv. 6*, 41522–41531.

(63) Shao, L., and Lutkenhaus, J. L. (2010) Thermochemical properties of free-standing electrostatic layer-by-layer assemblies containing poly(allylamine hydrochloride) and poly(acrylic acid). *Soft Matter 6*, 3363–3369.

CHAPTER 2: SELF-CROSSLINKING P(APM-*CO*-AA) MICROSTRUCTURED THIN FILMS AS BIOMIMETIC SCAFFOLDS

Christal Zhou, Jing Zhao, Kevin Saem, Urooj Gill, Jose Moran-Mirabal and Harald D. H. Stöver

2.1 Abstract

In nature, cells reside within an extracellular matrix (ECM), consisting of intricate networks of collagen and other proteins, which provide biophysical/chemical signals to direct cell development and behaviour. Traditional methods of studying cell behaviour often involve using *in vitro* models because they are convenient and cost-effective, but many are 2-dimensional and thus not representative of *in vivo* conditions. In this work, a synthetic polyampholyte, poly(*N*-(3-aminopropyl)methacrylamide hydrochloride-*co*-acrylic acid) [p(APM_x-*co*-AA_y)], was coated onto pre-stressed polystyrene support films that were then thermally shrunken at 130-165^{o}C, with concomitant self-crosslinking of the polyampholyte. Self-crosslinking involved a two-step sequence of anhydride formation from pairs of adjacent acrylic acid units, followed by amide crosslinking through reaction with a primary amine on another chain. Attenuated reflectance infrared spectroscopy (ATR IR) was used to confirm the formation of anhydride and amide bonds during heating, and the resulting crosslinked scaffolds were shown to remain intact in cell culture media and basic solutions. Furthermore, the compressive stress from the shrinking polystyrene substrate wrinkled the polyampholyte surface layer, producing thin film scaffolds that could be used as mimics of the 3-dimensional ECM. Cell viability tests confirmed the non-cytotoxicity of the microstructured films. The surface wettability of the films was tuned by post-functionalizing with different amines, with decylamine-

functionalized films showing decreased fibroblast attachment, and D-glucamine-functionalized films showing less fibroblast spreading compared to the control. The topography of the p(APM-*co*-AA) scaffolds was tuned by changing the polyampholyte film thickness. Different topographies of the microstructured films elicited different fibroblast morphologies, with larger wrinkle structures contributing to less complex cell boundaries, lower cell areas, and higher cell circularities. Overall, this tunable, self-crosslinking p(APM-*co*-AA) system can be fabricated into microstructured films, which can be used to gain insight on the effects of surface chemistry, topography, and other properties of the ECM on cell behaviour and contribute to the current library of biomimetic scaffolds.

2.2 Introduction

The ECM, the non-cellular constituent within all tissues, provides cells with physical scaffolding as well as biochemical/biomechanical cues necessary for tissue morphogenesis and differentiation.[1] The ECM guides the morphological organization and physiological function of cells, binds biomolecules such as growth factors, and maintains extracellular homeostasis.[1] The major components of the ECM are water, proteins, and polysaccharides. Genetic abnormalities in the ECM are responsible for a variety of diseases, such as osteogenesis imperfecta, Marfan's syndrome, and other genetic disorders.[2] Changes in the ECM can also lead to more common disorders such as coronary heart disease, in which the ECM binds excessive amounts of lipoproteins, resulting in atherosclerotic plaque formation.[2] Thus, finding ways to prevent or treat

cardiovascular diseases requires studying and understanding the ECM of diseased vessel walls. In addition, the ECM plays a crucial role in the progression of tumours, which has been associated with defects in the normal wound repair process.[3,4] Tumours are stiffer than healthy tissue due to increased deposition of ECM proteins such as collagen I,[3,5] and the increase in chemokines and growth factors, such as vascular endothelial growth factor (vEGF), promotes vascular permeability and tumor growth.[6] These changes in ECM stiffness and composition contribute to a positive feedback loop that ultimately induces angiogenesis and metastasis.[7] The importance of the ECM in biology and medicine has prompted the development of biomimetic scaffolds to study the ECM and cell behaviour *in-vitro* in biologically-relevant environments.

The ECM has been imitated through a variety of approaches to better understand how its fundamental biochemical and biophysical properties govern the molecular mechanisms of cell behaviour.[1] For example, Matrigel™, a reconstituted basement membrane derived from mouse carcinoma, has the ability to retain stem cells in an undifferentiated state and is commonly used to study cell differentiation, angiogenesis, and tumour growth.[8,9] However, its composition is not well-defined and this can lead to variability in experimental results.[8] Other natural scaffolds such as Type I collagen scaffolds can mimic some of the biological aspects of the ECM, however, have high levels of heterogeneity, which can greatly impact their porosity and organization.[10,11,1] While natural ECM mimics recapitulate some of the physical and biological properties of the native ECM, they are often not fully defined. Synthetic scaffolds from polymers have been developed to address the issue of reproducibility and tunability by providing well-

defined chemical and physical properties.[12,13] For example, hydrogels of acrylated polyethylene glycol could be grafted with cell adhesive peptides to support cell adhesion and growth.[12] Synthetic polymer hydrogels can also be functionalized chemically or by enzymatic reactions to tune their surface chemistry and better mimic the physiochemical properties of the ECM.[13] 2D polymer scaffolds however, fail to exhibit the organization and physical motifs that mimic natural collagen networks in the ECM.[1] Thus, the most recent developments of ECM mimics in the field involve scaffolds whose properties can be strictly controlled, including their fiber or structure size, stiffness, orientation, and surface chemistry.[12]

Microstructured polymer films can provide high surface areas and 3D environments that can be used as tunable ECM mimics for cellular scaffolds. A simple and inexpensive bench-top technique has been developed previously to fabricate a variety of micro/nanostructured surfaces.[14-17] This technique relies on the thermal shrinking of commercially available pre-stressed polystyrene (PS) films. Heating pre-stressed PS above its T_g (90^{o}C), but below its melting temperature (240^{o}C), shrinks the film down to 16% of its pre-heated area as a result of polymer chain relaxation.[14-16,18] If the PS substrates are coated with another polymer, this shrinking introduces 2D compressive stresses that wrinkle and buckle the coatings, generating micro/nanostructured surfaces.[14] As these films shrink biaxially, the interference of wrinkles in the x-y plane results in random wrinkling.[18] In this study, a polyampholyte formed by free radical copolymerization of N-(3-aminopropyl)methacrylamide hydrochloride and acrylic acid [p(APM-*co*-AA)] in a 10:90 mol ratio was spin-coated from aqueous solution onto pre-

stressed PS, dried, and then thermally wrinkled with simultaneous covalent crosslinking to form microstructured films. These films were then used to study the effect of the chemical and physical properties on the attachment and morphology of murine 3T3 fibroblasts.

p(APM-*co*-AA) thermally self-crosslinks without the need for potentially cytotoxic small molecule crosslinkers, and simultaneously forms reactive anhydride groups that allow for post-functionalization (Figure 2.1a).[19] The self-crosslinking allows the structured films to retain their shape in aqueous media, and the availability of anhydride groups after heating allows post-modification using nucleophilic groups (*e.g.,* nucleophilic amines). Post-functionalization can be useful since proteins, such as fibronectin and vitronectin, have been shown to mediate focal adhesions of cells to surfaces.[20] The type, quantity, and conformation of proteins adsorbed onto a material greatly depend on its surface charge and wettability. Thus, modifying chemical and physical properties of biomimetic scaffolds through functionalization is important in manipulating and studying cell behaviour. The ability to fine tune the composition, surface chemistry, and wettability of the p(APM-*co*-AA) system makes it a promising candidate for biomimetic scaffolds used to study cell biology.

In this study, p(APM_{10}-*co*-AA_{90}) was used to construct microstructured thin films, as this comonomer ratio offers a good balance between having a high incidence of adjacent acrylic acid units needed to form anhydride groups, and having sufficient amine-bearing comonomer to form amide crosslinks by reaction with these anhydrides. The crosslinking was characterized by scanning electron microscopy (SEM), attenuated total

reflectance infrared spectroscopy (ATR IR), thermogravimetric analysis (TGA), and solubility tests under Dulbecco's Modified Eagle Medium (DMEM) with bovine calf serum (BCS) or 1 mM NaOH. The surface chemistry of p(APM-*co*-AA) films was tuned by functionalizing the scaffolds with decylamine or D-glucamine, to modify their hydrophilicity.[25] Murine 3T3 fibroblasts were seeded onto the scaffolds to investigate the effects of microstructured film topography and surface chemistry on cell behaviour. The aim of the work is to explore the use of these tunable, self-crosslinking p(APM-*co*-AA) microstructured scaffolds as ECM mimics to study cell behaviour in biomimetic environments.

2.3 Results and Discussion

2.3.1 Synthesis and fluorescent labeling of p(APM_{10}-*co*-AA_{90})

P(APM_{10}-*co*-AA_{90}) was prepared by free radical batch-copolymerization as reported previously (Figure 2.1a and Supplementary Figure 1).[19] After dialysis to remove residual monomer, ^{1}H NMR showed no vinyl monomer peaks present, indicating successful purification (Supplementary Figure 2). The ^{1}H NMR also indicated the cumulative composition of the polymer as 9.3% APM and 90.7% AA, close to the targeted values. Gel permeation chromatography (GPC) showed M_n and M_w of 221 and 366 kDa respectively, with a dispersity of 1.7. Some batches were labelled by reaction with rhodamine B isothiocyanate in DMF (0.5% amine labeling).[19,21]

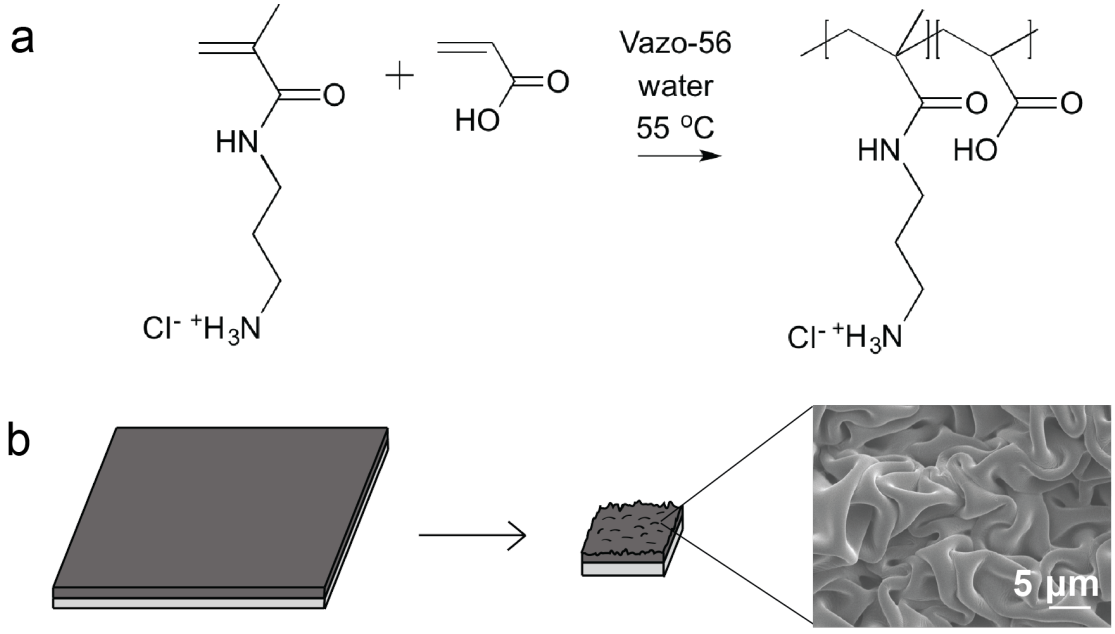

Figure 2.1. Synthesis and wrinkling of p(APM$_{10}$-*co*-AA$_{90}$) polyampholyte. a) Free radical co-polymerization of APM and AA monomers to form p(APM-*co*-AA). **b)** Microstructured films formed by thermal shrinking of a polystyrene substrate.

2.3.2 Fabrication and Characterization of Structured Films

Figure 2.1a illustrates the copolymerization of APM and AA to form the polyampholyte copolymer, and its subsequent deposition onto pre-stressed polystyrene and thermal shrinking to form wrinkled polyampholyte surfaces (Figure 2.1b). Specifically, aqueous solutions of p(APM$_{10}$-*co*-AA$_{90}$) at 2, 4, 6, 8, and 10 wt% were spin-coated to form films of increasing thickness (Figure 2.2a-b). Heating these films at 130^{o}C for 15 minutes led to a series of randomly wrinkled films with the wavelength of wrinkling increasing with film thickness (confocal images, Figure 2.2a), as had been reported previously.[16] The appearance of wrinkles with defined wavelength and amplitude is characteristic of compression with buckling instability, and implies different Young's moduli of p(APM$_{10}$-*co*-AA$_{90}$) and PS.[22]

The water contact angles of the structured films as a function of wt% of spincoating solution were investigated (Figure 2.2c). After thermal treatment, which introduces hydrophobic anhydride groups into the copolymer, the water contact angles of both as-formed and hydrolyzed films were measured. Contact angles for the unhydrolyzed structured films were similar at about 125^{o}, while the hydrolyzed films showed overall much lower contact angles, with a tendency to increase with film thickness/wrinkle dimension.

These results indicate that p(APM$_{10}$-*co*-AA$_{90}$) can be structured uniformly on PS without delamination or cracking, even at large wrinkle wavelengths, and the morphology of the films can be tuned by changing the wt% of spin-coated polymer solution.

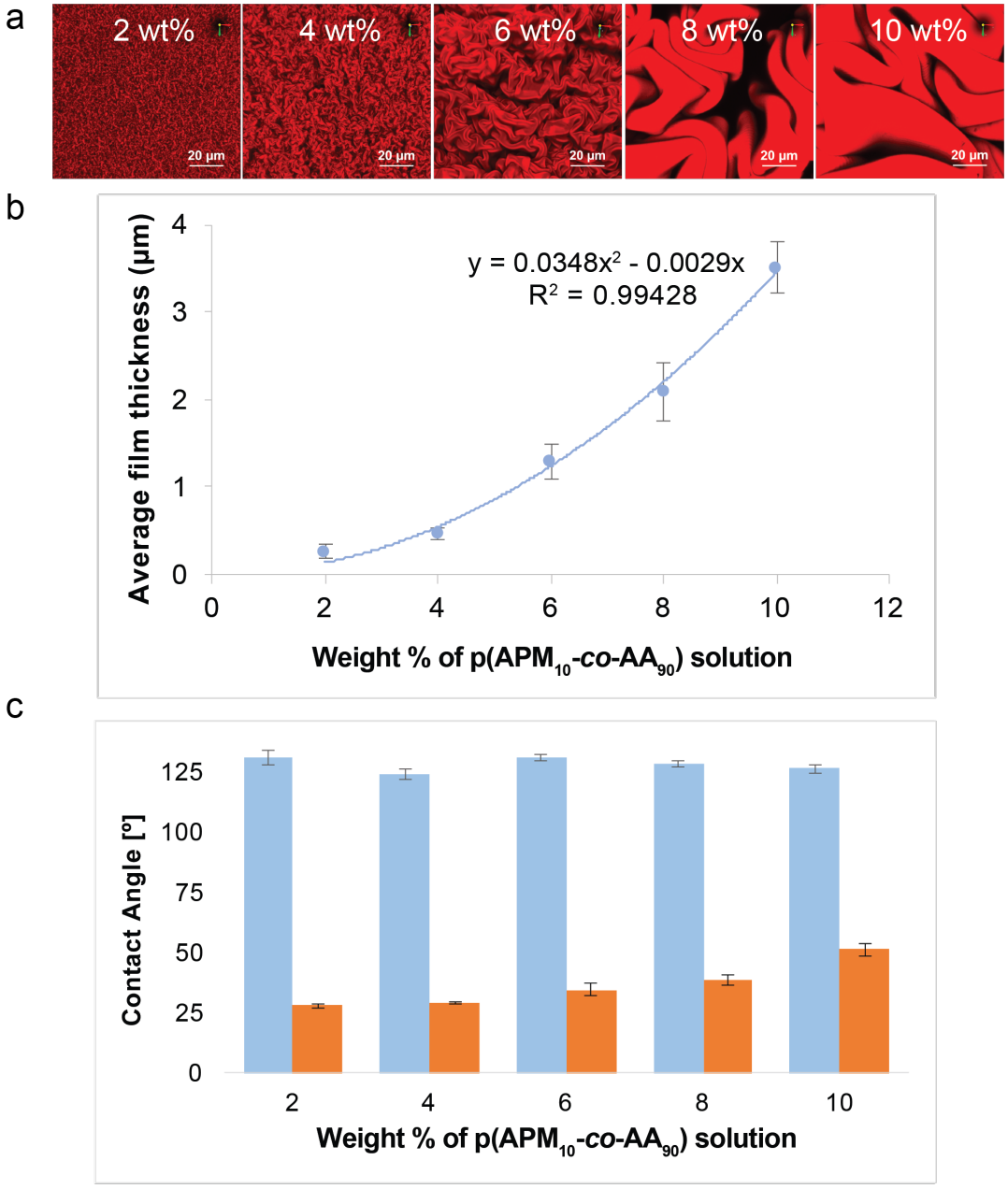

Figure 2.2. Wrinkling features and flat film thickness as function of polyampholyte spincoating solution wt%. a) Confocal microscopy (3D rendered z-stack) images of 2, 4, 6, 8, 10 wt% of microstructured p(APM_{10}-*co*-AA_{90}) films. **b)** Average film thickness as function of wt% of p(APM_{10}-*co*-AA_{90}) spincoating solution. Solid line represents the trendline fitted to the data (second order polynomial). **c)** Water contact angles of unhydrolyzed (blue) or hydrolyzed (orange) structured films as a function of wt% of p(APM_{10}-*co*-AA_{90}) spincoating solution.

2.3.3 Covalent Crosslinking and Characterization

It had previously been observed that p(APM_{10}-*co*-AA_{90}) heated in the dry state would subsequently swell but not dissolve back into solution (J. Zhao, private communication). This was attributed to self-crosslinking, plausibly through a two-step process of anhydride formation between adjacent acrylic acid groups, followed by amide crosslinking with amines on other chains (Figure 2.3e). This process, if integrated with the thermal shrinking of the pre-stressed PS substrate coated with p(APM_{10}-coAA_{90}), could lead to both microstructured and crosslinked surfaces which could then be used directly in aqueous environments, including as cellular scaffolds, without dissolution.

Using this inherent thermal self-crosslinking ability of p(APM_{10}-*co*-AA_{90}) obviates the use of potentially cytotoxic small molecule crosslinkers, and streamlines the overall process. The most uniform film surfaces were obtained with a two-step thermal protocol consisting of an initial 15 minute heating at 130^{o}C to shrink the PS substrate,[14] followed by an additional 45 minute heating at 165^{o}C to complete the covalent crosslinking of the wrinkled film. The formation of amide bonds in the p(APM_{10}-*co*-AA_{90}) system was confirmed by ATR IR (Figure 2.3a).

A series of thermal protocols was explored to assess the relative rates of crosslinking versus thermal treatment. ATR IR spectra of unheated and heated bulk samples of p(APM_{10}-*co*-AA_{90}) and pAA (control) were obtained, after treatments of: 130^{o}C for 15 minutes (130/15), 130^{o}C for 15 minutes plus 165 ^{o}C for 15 minutes (165/15), 130^{o}C for 15 minutes plus 165^{o}C for 30 minutes (165/30), 130^{o}C for 15 minutes plus 165^{o}C for 45 minutes (165/45), or 130^{o}C for 15 minutes plus 165^{o}C for 45 minutes

plus 180°C for 15 minutes (180/15). The spectra from the five replicates were averaged and overlaid for comparison. After heating pAA, peaks at 1800 cm^{-1} and 1030 cm^{-1} appear, which come from one of the C=O bonds of the anhydride and the C-O-C bending vibrations of the anhydride respectively, confirming anhydride formation (Supplementary Figure 3). This is congruent with the literature, which reported on the heating of pAA at 200°C, however our peaks were weaker, possibly due to the lower temperature and shorter heating time.[23,24] Nonetheless, heating for 165/45 was enough to form some anhydrides from pAA.

Comparison of the spectra of unheated and heated p(APM_{10}-*co*-AA_{90}) confirms that amide formation occurred at 165°C, as indicated by the increased intensity of the amide I peak at 1650 cm^{-1} (Figure 2.3a). There was also an increase in the C-O-C peaks at 1030 cm^{-1} from anhydride formation. However, the signal from the anhydride C=O peak at 1800 cm^{-1} was much weaker than for pAA. This could be caused by a combination of the reduced ability for p(APM_{10}-*co*-AA_{90}) to form anhydrides due to the presence of APM units, in addition to some anhydrides lost by reacting with amines to form amide crosslinks. Peaks were normalized to the strongest peak at 1700 cm^{-1}. Quantitative analysis was performed on the averaged spectra by analyzing the differences in intensities (Supplementary Figure 4). The percent increase of the amide I peak of the 160/45 heated polymer relative to the unheated polymer was 10%, as expected from 9.3% APM content.

Previous work in our group has shown that heating p(APM_{10}-*co*-AA_{90}) led to polymers that could be swollen, but did not dissolve at any pH, which is consistent with the amide formation indicated by ATR IR. The crosslinking mechanism proposed

involves adjacent AA units dehydrating to form anhydrides (Figure 2.3e), followed by amines from APM units in a neighbouring polymer chain reacting with the anhydride to provide intermolecular crosslinking. SEM was used to investigate whether there were any morphological differences between the structured films during the different heating stages and none were observed, indicating that the covalent crosslinking does not lead to noticeable changes in film morphology (Supplementary Figure 5). Overall, the ATR IR spectra confirm that heating p(APM_{10}-*co*-AA_{90}) results in the formation of amide bonds.

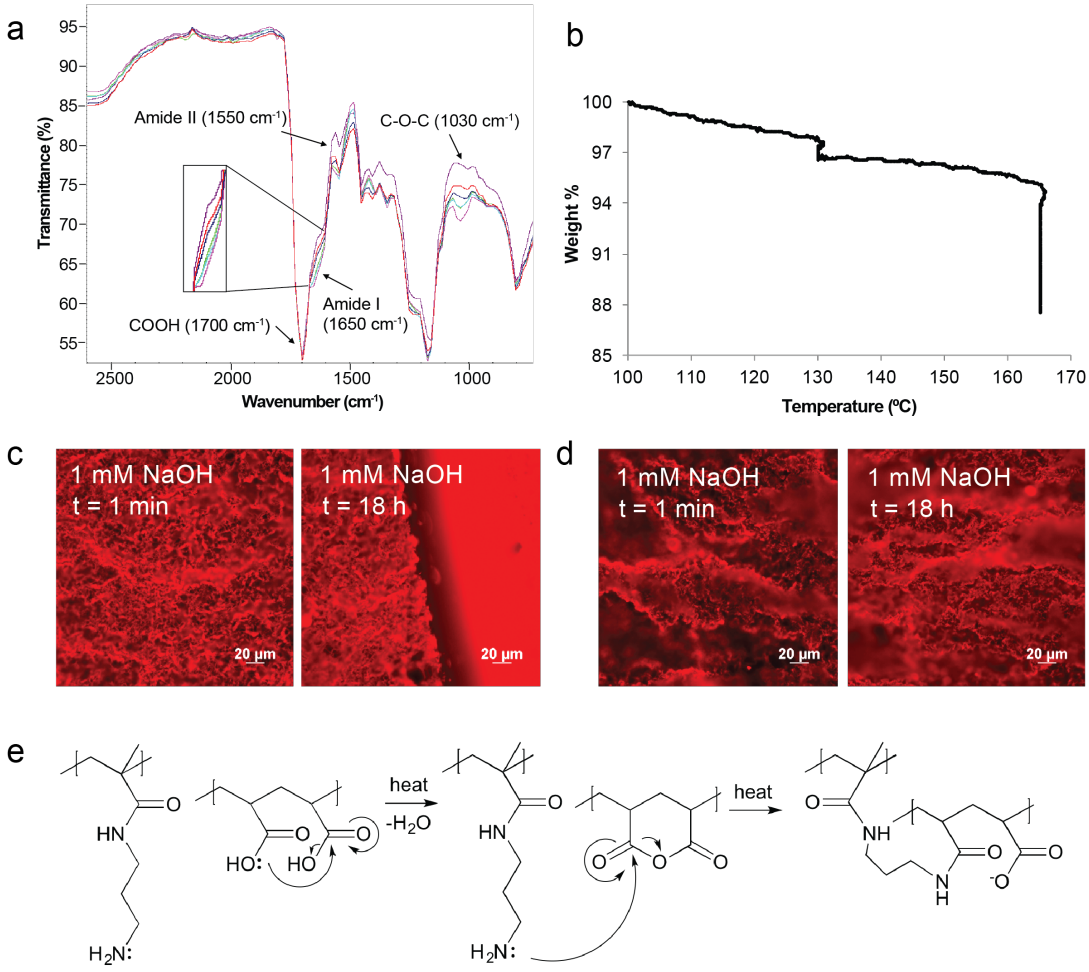

Figure 2.3. Characterization of covalent crosslinking through a) ATR IR, b) TGA, c)-d) solubility tests and e) proposed mechanism of crosslinking. a) ATR IR spectra of unheated and heated p(APM_{10}-*co*-AA_{90}) bulk polymer were obtained, with five replicates per sample, with treatments of: unheated (purple), 130°C for 15 minutes (130/15, red), 130°C for 15 minutes plus 165 °C for 15 minutes (165/15, navy), 130°C for 15 minutes plus 165°C for 30 minutes (165/30, green), 130°C for 15 minutes plus 165°C for 45 minutes (165/45, teal), or 130°C for 15 minutes plus 165°C for 45 minutes plus 180°C for 15 minutes (180/15, pink). Overlay of averaged spectra suggest that majority of amide formation occurred when heating above 165°C, displayed by the increased intensity of the amide I peak at 1650 cm^{-1}. There was also an increase in the C-O-C peaks from anhydrides at 1030 cm^{-1}. **b)** TGA was performed by increasing the temperature by 5°C/min until 130°C, held constant for 15 min, increased to 165°C, and held constant for 45 min, mimicking the crosslinking procedure. The loss in mass starting from 100°C to 165°C was calculated to be a ~12% mass loss, which matches the predicted loss of mass from water during the crosslinking reaction. **c)** Solubility tests in 1 mM NaOH of 130/15 or **d)** 165/45 heated 2 wt% p(APM_{10}-*co*-AA_{90}) structured films. Unheated p(APM_{10}-*co*-

AA_{90}) films dissolved immediately (not shown). In contrast, all of the heated scaffolds survived the solubility tests. The straight lines represent scratches made on the film for visualization. **e)** Proposed mechanism of polyampholyte crosslinking: adjacent acrylic acid units dehydrate to form anhydride moieties. The amine from the APM unit can then attack the anhydride to form intermolecular crosslinks.

Thermogravimetric analysis (TGA) was performed on bulk p(APM_{10}-*co*-AA_{90}) and pAA to investigate whether there was a measurable loss of water during the crosslinking procedure, as well as to determine when degradation of the polymer occurs. A preliminary TGA of p(APM_{10}-*co*-AA_{90}) and pAA indicated that degradation of the polymer did not occur below 200^{o}C, confirming that the crosslinking procedure at 165^{o}C does not destroy the polymer (Supplementary Figure 6). Thus, our crosslinking procedure was kept at a temperature of 165^{o}C for 45 minutes. In an effort to mirror the conditions used for shrinking and crosslinking of the polyampholyte films, TGA was performed on p(APM_{10}-*co*-AA_{90}) where the temperature was increased at 5^{o}C/min until 130^{o}C, held constant for 15 min, then increased to 165^{o}C, and held constant for 45 min, mimicking the crosslinking procedure that the p(APM_{10}-*co*-AA_{90}) films were subjected to (Figure 2.3b). The loss in mass starting from 100^{o}C to 165^{o}C was calculated to be a ~12% mass loss, which matches the ~10% predicted loss of mass from water during the crosslinking reaction. Another TGA was performed to investigate isothermal mass loss, where the temperature was increased at 10^{o}C/min and held constant at 165^{o}C for 2 h. The initial mass loss was due to loss of bound water, which started to plateau at ~100^{o}C, while the mass loss that occurred after, at 165^{o}C for ~2 h, was approximately ~8%, in agreement with the predicted mass loss from crosslinking (Supplementary Figure 7). Overall, the TGA results indicate that the polymer does not degrade during the crosslinking procedure

and that the loss of mass during the heating corresponds to the loss of water from the formation of anhydrides, supporting our proposed mechanism of crosslinking.

To investigate whether the amide crosslinking shown by ATR IR was sufficient to prevent dissolution, microstructured p(APM_{10}-*co*-AA_{90}) films formed using 130/15, 165/15, 165/30, and 165/45 protocols were submerged into either 1 mM NaOH (Figure 2c-d) or DMEM with 10% Bovine Calf Serum (BCS) (incubated in 5% CO_2) for 18 h (Supplementary Figure 8). Unheated p(APM_{10}-*co*-AA_{90}) films dissolved immediately in either media. In contrast, all of the heated scaffolds withstood the solubility tests. Fluorescence images showed no notable differences in film morphology or swelling between the differently heated films. This suggests that even small amounts of crosslinking can effectively suppress macroscopic swelling under these conditions. Overall, the heated films stayed intact despite being submerged in DMEM and 1 mM NaOH, indicating that the crosslinking provided the films with sufficient structural integrity to withstand harsh conditions.

2.3.4 Functionalization of Films with Decylamine and D-glucamine

The presence of residual anhydride groups in the p(APM-*co*-AA) films after heating suggests they might be post-modified using amines. For example, decylamine or D-glucamine can be reacted with the anhydrides in methanol to modify the hydrophilicity of the surface.[25] Both flat and microstructured films were functionalized with different amines to modify the surface wettability immediately after crosslinking. Decylamine was used to increase the hydrophobicity of the films while D-glucamine was used to increase

the hydrophilicity of the films (Figure 2.4a). D-glucamine has been previously reported to convey antifouling properties, such as decreased cell attachment.[13,25] The depth of functionalization was investigated using fluorescein cadaverine and confocal microscopy, with the fluorescence from the functionalized films suggesting that these small molecules were able to penetrate and functionalize the whole film (Supplementary Figure 9). The ability to modify the physiochemical properties of the preformed polymer films is an important attribute in biomimetic scaffolds, since it may allow for the manipulation and study of specific cell behaviour, such as stem cell pluripotency or differentiation.[26]

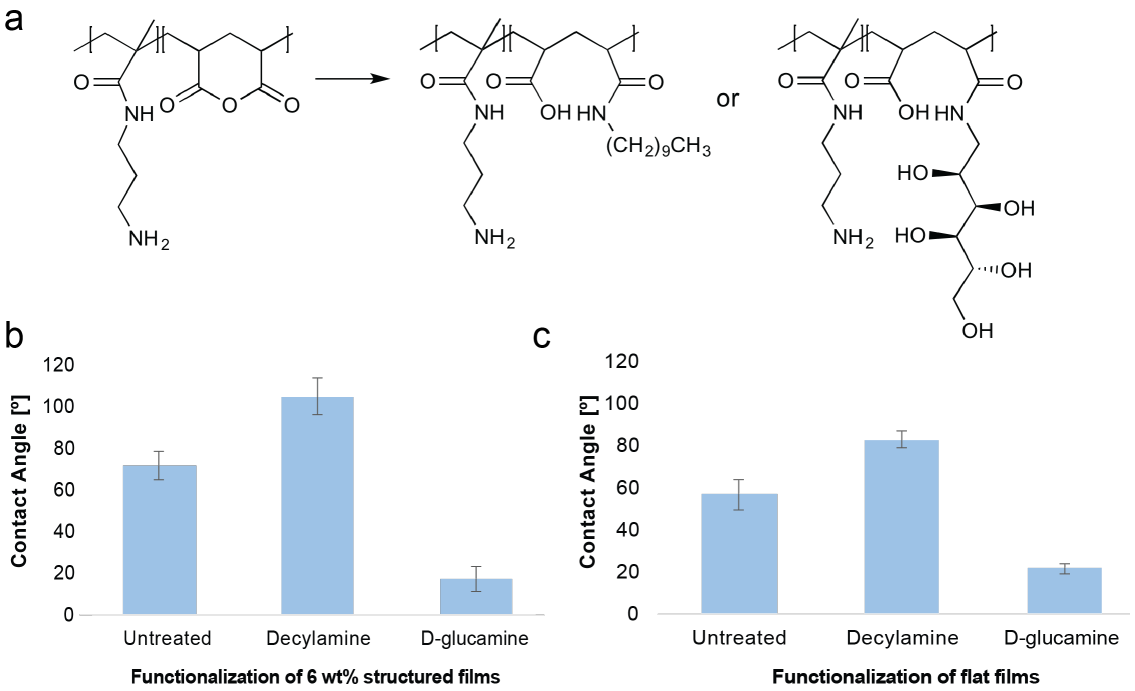

Figure 2.4. Decylamine and D-glucamine were grafted onto microstructured and flat polymer films. a) Modification of the surface chemistry and wettability of scaffolds by reacting the anhydride moieties of p(APM_{10}-*co*-AA_{90}) with amines. **b)** Water contact angles of decylamine and D-glucamine functionalized 6 wt% structured films. **c)** Water contact angles of decylamine and D-glucamine functionalized flat films. Error bars represent standard deviations of replicate measurements, n = 3.

Water contact-angle data were obtained and suggest that the grafting of the different amines on the structured and unstructured flat films was successful (Figure 2.4b-c). For the 6 wt% structured films, the untreated film displayed an average contact angle of 71 ± 6°, while the angles for the decylamine and D-glucamine functionalized films were 104 ± 9° and 17 ± 6°, respectively. For the flat films, the untreated control displayed an average contact angle of 57 ± 7°, while the angles for the decylamine and D-glucamine functionalized films were 83 ± 4° and 21 ± 2°, respectively. The ability to modify the surface chemistry and wettability of these films is an advantage in the development of tunable cellular scaffolds. The natural ECM is loaded with ligands, peptides and growth factors.[1] The successful functionalization of these films with simple small molecules bearing amine moieties opens up the possibility of post-functionalizing with biomolecules to better represent different stages of ECM remodelling for different tissues and/or cell lines.

2.3.5 Effects of Film Surface Chemistry and Topography on Fibroblast Morphology

Murine NIH 3T3 fibroblasts were used as model cells to investigate the cytotoxicity of the microstructured surfaces and the morphologies that cells exhibited on them. Approximately 90% or more of the cells that attached onto the surfaces were viable after 22 hours incubation, as assayed through live/dead fluorescence cell staining, which suggests that the films are non-cytotoxic and suitable as cellular scaffolds (Supplementary Figure 10). The effects of surface chemistry of flat p(APM_{10}-*co*-AA_{90}) films on fibroblast cell morphology were investigated using fluorescence microscopy. Fibroblasts were

seeded onto films as-prepared or after functionalization with decylamine or D-glucamine, and incubated overnight prior to staining with DAPI for nuclei, and Alexa Fluor 488 phalloidin for actin filaments. Representative images of the fibroblasts on PS and the flat polyelectrolyte films were taken on a fluorescence inverted microscope (Figure 2.5a). Compared to the PS control, fibroblasts on the flat p(APM_{10}-*co*-AA_{90}) films were less spread out onto the surface and exhibited smaller cell areas. It was previously reported that fibroblasts tend to adopt more circular and evenly spread out morphologies on more hydrophilic surfaces.[20] Thus, these results were expected since the p(APM_{10}-*co*-AA_{90}) surface is more hydrophilic than the PS control. Fibroblasts on the D-glucamine functionalized p(APM_{10}-*co*-AA_{90}) films were the least spread out and most circular. D-glucamine is known to have anti-fouling properties because the surface is too hydrophilic and prevents proteins from binding, significantly reducing cell attachment.[27] There were little to no cells on the decylamine functionalized films after washing, suggesting that there was limited cell adhesion to these films. This is in contrast to earlier work where decylamine functionalization of anhydride-functional surfaces led to enhanced 3T3 cell attachment.[25] However, it has been reported that hydrophobic surfaces pre-adsorbed with serum or bovine serum albumin (BSA) show little fibroblast attachment.[20] BSA on hydrophobic surfaces show limited binding activity to its antibody, antialbumin, suggesting the protein denatures on hydrophobic surfaces.[27] The hydrophobic decylamine chains on the surface of the films could have been too hydrophobic, and possibly denatured the proteins required for cell attachment. These results demonstrate that the surface chemistry and ability for cell attachment of our p(APM-*co*-AA) system can be

tuned by functionalizing the films with different amine-bearing molecules, though more studies are needed to explore these effects in more detail.

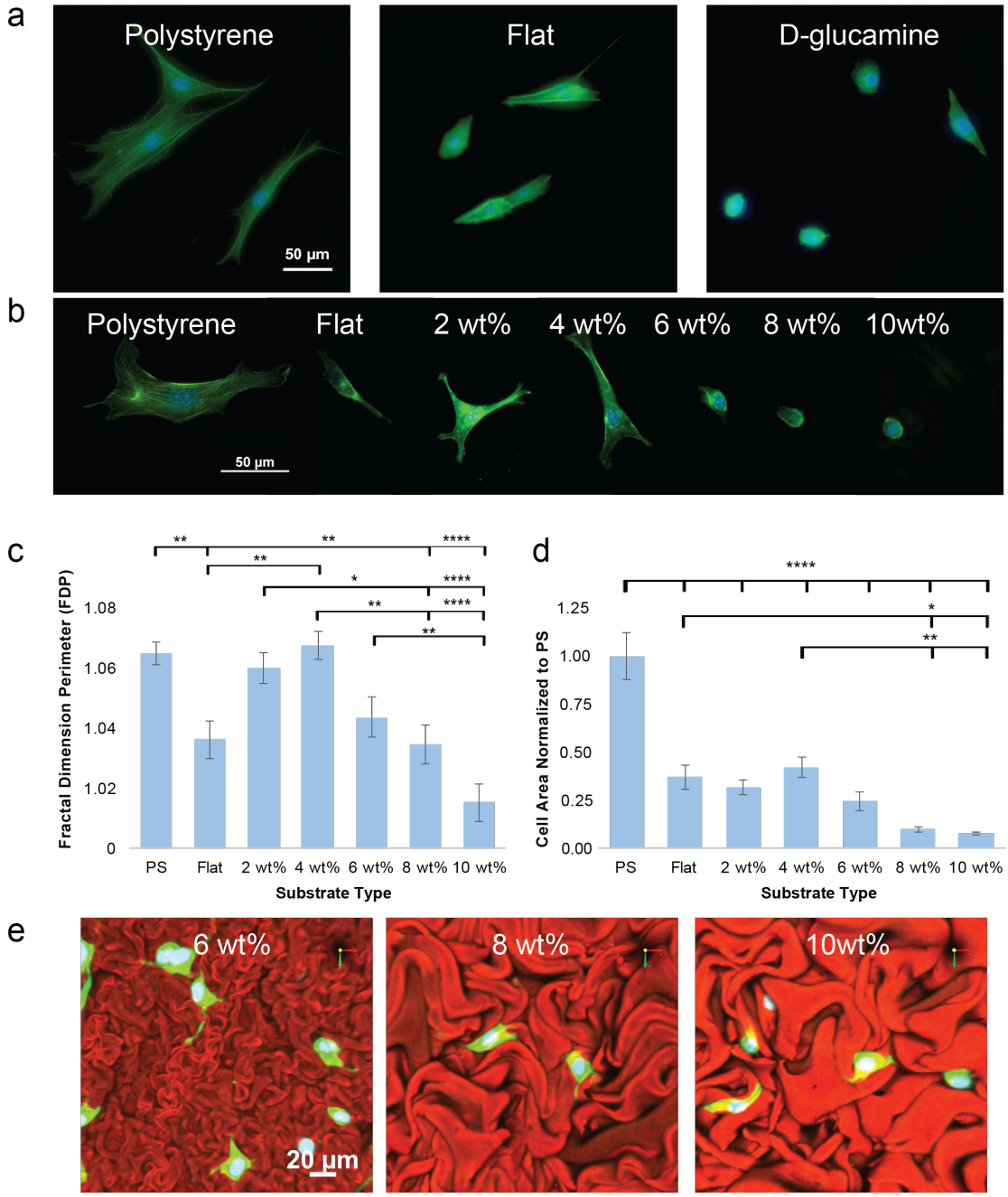

Figure 2.5. The effects of surface chemistry and microstructured film topography on fibroblast morphology were studied using fluorescence microscopy. a) Fibroblasts were seeded onto polystyrene control, unfunctionalized or D-glucamine functionalized flat p(APM_{10}-*co*-AA_{90}) films. Compared to the PS, fibroblasts on the flat p(APM_{10}-*co*-AA_{90}) films were less spread out onto the surface and exhibited smaller cell areas. Fibroblasts on the D-glucamine functionalized p(APM_{10}-*co*-AA_{90}) films were the least spread out and most circular. **b)** Fibroblasts were seeded onto polystyrene, flat p(APM_{10}-

co-AA_{90}) films, or structured 2 wt%, 4 wt%, 6 wt%, 8 wt%, and 10 wt% p(APM_{10}-*co*-AA_{90}) films. Compared to the PS, fibroblasts on the structured films were less spread out onto the surface and exhibited smaller cell areas. As structure size increased further, cells exhibited a circular morphology. **c)** The fractal dimension perimeters (FDPs) and **d)** areas of the cells were obtained using MATLAB and ImageJ. Among the structured polymer films, increasing the size of the structures resulted in a general decrease in FDPs, suggesting cells generated less filopidia on the larger structures. Analysis of variance (ANOVA for all data sets) was performed on Prism (* = $P \leq 0.05$ ** = $P \leq 0.01$ *** = $P \leq 0.001$**** = $P \leq 0.0001$). **e)** On structured films of 6 wt% or greater, the grooves were large enough for cells to embed into. In a-b), fibroblasts were stained with DAPI and Alexa Fluor 488 phalloidin while in e), fibroblasts were stained with NucBlue® Live ReadyProbes® Reagent and calcein-AM.

The effect of substrate topography on fibroblast cell morphology was also investigated using fluorescence microscopy. Fibroblasts were seeded onto films prepared from solutions with different polymer wt% to vary the surface topography, and were incubated overnight prior to staining and visualization (Figure 2.5b). Representative images of the fibroblasts on PS and flat or structured polymer films were used for analysis. Quantitative analysis on the fibroblast cell boundaries was performed using a box counting method of fractal analysis on each cell.[28] The fractal dimensions of perimeter (FDPs) of the cells were obtained to investigate cell boundary complexity. The FDPs were calculated by a program on MATLAB that plots the number of boxes needed to cover the perimeter of each cell against the size of the boxes.[29] The resulting slope of this line represents the fractal dimension; a larger FDP, or a larger slope, corresponds to a perimeter that gains in complexity as box size decreases. The FDPs, cell areas (Figure 2.5c-d) and cell circularities (Supplementary Figure 11) were analyzed from the binary maps of the cell images. The ability to study cell morphology as function of film topography can be a useful tool in studying cell responses to different ECMs.

Cells on the flat polymer substrate control displayed lower FDPs and smaller areas than the cells on the PS control, indicating that cells on the polymer surface generated fewer filopodia and attachment points. This was attributed to the polymer being more hydrophilic than the PS, preventing proteins required for attachment, such as collagen and fibronectin, to bind onto the surface.[20] The optimal contact angle for cell attachment has been reported to be around 70 – 80°,[27] however, the flat polymer has a slightly lower contact angle of 57 ± 7°. On the 4 wt% microstructured films, cells displayed higher FDPs and cell areas than cells on flat polymer and 2 wt% films, indicating that they generated more filopodia despite being exposed to the same surface chemistry. These upward trends highlight the effect of topographical features on adhesion, where a larger available surface area can lead to more protein adsorption and cell attachment points. However, on structured films of 6 wt% or greater, downward trends in the FDPs and cell areas are observed. The wrinkles in 6, 8, 10 wt% films were large enough for cells to embed within the grooves, instead of spread across them (Figure 2.5e), explaining the smaller FDPs, smaller cell extension and significantly larger cell circularities. The observation of cells aligning and embedding into grooves has been widely reported in the literature.[30] Fibroblasts are known to be able to conform and align along microfabricated grooves through contact guidance. There are several proposed mechanisms for the induction of contact guidance, as the mechanisms of how cells sense and respond to surface topography are still largely unknown.[31] The most common mechanism suggests that microtubules are the first cellular element to orient parallel to the grooves of the substrate, followed by actin microfilaments, and then focal adhesions.[31] Since the

cytoskeleton component of the cell is initially aligned to the grooves, it ultimately determines the cell orientation and causes the cell to align to the structures. In the natural ECM, collagen fibrils, which range in diameters of 20-200 nm, form collagen fibers whose nano/microstructures influence the polarity and migration of cells through contact guidance cues.[31] Furthermore, cells on all microstructured surfaces were less spread out and exhibited smaller cell areas. These observations are congruent with previous studies with human fibroblasts on structured polydimethylsiloxane (PDMS) scaffolds, in which the fibroblasts on PDMS structured scaffolds exhibited a decreased tendency to adhere and spread compared to cells on flat PDMS, requiring less force to remove them with the atomic force microscope.[32] Cells cultured on flat surfaces are reported to face more cytoskeletal stress and display more stress fibers.[33] With smaller cell areas and less focal adhesions to hinder the dynamic nature of the ECM, the cells on the structured surfaces better mimic the cells observed *in vivo* than cells on flat substrates.[32] These results indicate that our structured surfaces offer topographical cues that regular 2D substrates cannot, causing cells to exhibit morphologies that are more representative of *in vivo* conditions. Hence, the topography of the microstructured p(APM_{10}-*co*-AA_{90}) scaffolds can be tuned to elicit specific fibroblast morphologies and study the effect of topographical features on cell behaviour in more biologically-relevant environments.

2.4 Conclusion

Overall, p(APM_{10}-*co*-AA_{90}) can be successfully fabricated into microstructured thin films by shrinking using pre-stressed PS as a substrate, allowing for the fabrication of 3D

scaffolds of different topographies. ATR IR spectra and solubility tests in DMEM and 1 mM NaOH indicate that the p(APM_{10}-*co*-AA_{90}) scaffolds successfully self-crosslinked under heat without the use of small molecule crosslinkers, permitting their use as ECM mimics in aqueous environments. Cell viability tests confirmed the suitability of cell culture on the substrates. The surface wettability of the flat and structured films was successfully modified by functionalizing residual anhydride groups in the films with either decylamine or D-glucamine, which elicited different cellular morphologies. Fractal analysis on the cell perimeters of murine fibroblasts seeded onto films prepared with different topographies suggest that larger structures contributed to more circular cell shapes and decreased cell areas due to cells embedding into grooves. These results demonstrate the ability to fine tune topography to affect cell morphologies, another property of the microstructured scaffolds that can be tuned to manipulate cell behaviour.

Future work includes using different compositions of p(APM-*co*-AA) to vary crosslinking capacity and the elastic moduli of the films. Furthermore, it has been reported that structured films can influence fibroblast motility, with larger structures leading to decreased motility.[34] The effect of the structured films on fibroblast motility could be investigated directly through confocal microscopy. Overall, our p(APM-*co*-AA) system can be used in a variety of applications, including as cellular scaffolds to study cell biology, and its chemical and physical tunability makes it a great candidate in probing specific cellular responses, providing a new tool to study and understand the ECM and its properties.

2.5 Materials and Methods

2.5.1 Synthesis of p(APM_{10}-*co*-AA_{90}).

p(APM_{10}-*co*-AA_{90}) was prepared as reported previously by free radical batch-copolymerization on a 2-g scale.[19] For a 2-g scale, APM hydrochloride monomer (432 mg, Polysciences, Warrington, PA), AA monomer (1.568 g, distilled before use, 99%, Sigma Aldrich), and 2,2'-azobis(2-methylpropionamidine) dihydrochloride (Vazo-56) (65.56 mg, 97%, Sigma Aldrich, Oakville, ON) were added to a 20 mL screw cap glass vial. Distilled water was added to the vial before placing the vial at 55^{o}C in an oven with horizontal steel rollers to rotate for 30 minutes. Ethylene carbonate (10 mg/mL, 98%, Sigma Aldrich, Oakville, ON) in D_2O (Cambridge Isotope Laboratories, Andover, MA) was used as an internal NMR integration standard. Monomer conversion was analyzed by ^{1}H NMR on a Bruker Avance 200 spectrometer at room temperature. The vinyl peaks of APM monomer at 6.45, 6.20, 6.01 ppm and AA monomer at 5.48 and 5.73 ppm, before and after polymerization, were used to calculate the monomer conversion, and the cumulative composition, calculated as 9.3% APM and 90.7% AA. Polymerized mixtures were dialyzed in distilled water using cellulose tubing (Spectra/Por, 3.5 kDa MW cutoff, Spectrum Laboratories, Rancho Dominguez, CA) for five days with two water bath changes each day. The polymer solution was then freeze-dried, which yielded 1.64 g of polymer.

2.5.2 Labelling p(APM_{10}-*co*-AA_{90}) with rhodamine B isothiocyanate.

p(APM_{10}-*co*-AA_{90}) was covalently labelled with rhodamine B isothiocyanate (0.5% labelling). Rhodamine B isothiocyanate (0.05569 g, Sigma Aldrich) was dissolved in DMF (5.6 mL, Caledon). The polymer was dissolved in 0.1 M sodium bicarbonate buffer. The pH of the solution was adjusted to 9 with NaOH (LabChem Inc, Zelienople, PA). The rhodamine B isothiocyanate solution was added dropwise into the polymer solution, which was stirred vigorously. The reaction mixture was incubated and left stirring at room temperature for 1 h. After 1 h, the pH of the solution was adjusted to pH 7 with HCl (LabChem Inc, Zelienople, PA) to reduce swelling during dialysis. The solution was purified using dialysis against distilled water for five days, with water changes bath two times a day. The purified polymer solution was freeze-dried and yielded 1.3741 g of polymer.

2.5.3 Gel permeation chromatography (GPC) Analysis.

The molecular weight of the p(APM_{10}-*co*-AA_{90}) was estimated using aqueous gel permeation chromatography (GPC) setup consisting of Waters 515 HPLC pump, Waters 717 plus Autosampler, three columns (Waters Ultrahydrogel-120, -250, -500; 30 cm × 7.8 mm; 6 μm particles), and a Waters 2414 refractive index detector. The system was calibrated using narrow-dispersed PEG standards (Waters, Mississauga, ON). The mobile phase was 0.3 M $NaNO_3$ buffer. The reported M_n and M_w were 221,114 and 365,934 Da respectively, with a PDI of 1.65.

2.5.4 Fabrication of flat films.

p(APM_{10}-*co*-AA_{90}) was dissolved in a mixture of 20:80 MeOH:H_2O and the pH was adjusted to 2.8 with HCl while stirring at 37 ˚C for over 12 h. Pre-stressed polystyrene films, roughly 2 cm x 2 cm, (Graphix Shrink Film, Graphix, Maple Heights, Ohio) were cleaned with isopropyl alcohol, ethanol and water (5 min each) before drying with a dry nitrogen stream. The PS substrates were spincoated with either 2, 4, 6, 8, 10 wt% p(APM_{10}-*co*-AA_{90}) solutions by adding 20 µL of each solution onto the PS films and rotating at a speed of 4000 rpm for 30 s with a ramp of 7.0 s using a Spincoat G3P-12 (Specialty Coating Systems, Inc., Indianapolis, IN).

2.5.5 Shrinking and crosslinking procedure.

Polymer spincoated PS films were shrunken by heating at 130˚C for 15 minutes in an isotemp vacuum oven (Fisher Scientific, Ottawa, ON, Canada) on aluminum boats lined with parchment paper to prevent uneven shrinking, and cooled before heating them further at 165˚C for 45 minutes on a silicon wafer to ensure flattening of the substrates. The microstructured polymer films (2, 4, 6, 8, 10 wt%) were visualized in 1x PBS pH 7.4 using a Nikon A1 Confocal Eclipse Ti microscope with Nikon A1plus camera and Nikon Elements software (60x/1.4NA oil immersion lens).

2.5.6 White light interferometry flat film thickness measurements.

The films were spincoated with either 2, 4, 6, 8, 10 wt% p(APM_{10}-*co*-AA_{90}) solutions by adding 20 µL of each solution onto glass cover slips and rotating at a speed of 4000 rpm

for 30 s with a ramp of 7.0 s. A razor blade was used to create straight scratches on the films prior to surface profile characterization using a surface optical digital profilometer (Veeco Wyko NT1100, DYMEK Company Ltd., Tsuen Wan, Hong Kong) in vertical scanning interferometry (VSI) mode, equipped with a Accelevision LCDPH 5" Universal Monitor (Accele Electronics Inc., 12VDC voltage, Cerritos, CA, USA) to visualize the films. Ten different regions on each triplicate per sample were imaged at a magnification of 20.6 (20x objective) and an area of 227 x 299 um^2. Images were processed using the WYKO Vision32 software (Veeco instruments, Tucson, AZ) to provide line profiles in two areas of each image, which were used to calculate the average step-height differences representing average film thicknesses.

2.5.7 Attenuated Total Reflectance Fourier Transform Infrared Spectroscopy (ATR FT-IR).

Bulk polymer samples (~3 mg each replicate, five replicates per sample) of p(APM_{10}-*co*-AA_{90}) or pAA were heated for either 130/15, 165/15, 165/30, or 165/45 before immediately obtaining ATR FT-IR spectra of the solid polymer (n = 5) using a Thermo Nicolet 6700 (Thermo Electron Corporation, WI, USA) equipped with a Smart iTX ATR accessory and Omnic 8 data processing software at room temperature. Spectra of unheated polymer were also obtained as controls. Spectra were analyzed quantitatively on Microsoft Excel by calculating the averaged values (n = 5) of the amide I peak (1650 cm^{-1}) normalized to the strongest peak (1700 cm^{-1}).

2.5.8 Thermogravimetric analysis (TGA).

TGA measurements were obtained using a TGA Q50 (TA instruments, New Castle, DE). Bulk pAA or p(APM_{10}-*co*-AA_{90}) polymer (~5 mg each) was heated at a constant temperature ramp (5°C/min) from room temperature to 495°C and the change in mass was recorded. Another run was performed where the temperature was increased at 5°C/min until 130°C, held constant for 15 min, increased to 165°C, and held constant for 45 min to mimic the crosslinking procedure. This data was then replotted on Microsoft Excel. An isothermal run was performed where the temperature was increased at 10°C/min and held constant at 165°C for a total of 2 h.

2.5.9 Scanning electron microscopy (SEM).

Microstructured films (6 wt%) that were heated for either 130/15, 165/15, 165/30, or 165/45 were visualized through scanning electron microscopy (SEM), using a JEOL JSM-7000S (JEOL USA, Inc., Peabody, MA) scanning electron microscope. Images were taken at an accelerating voltage of 2.5 kV, working distance of 5.9-6.0 mm, and low probe current of 30 μA.

2.5.10 Solubility Tests in NaOH and DMEM.

Films that were heated for either 130/15, 165/15, 165/30, or 165/45 were submerged into either DMEM with 10% BCS and incubated with 5% CO_2 to mimic physiological conditions or water containing 1 mM NaOH to investigate the structural integrity and degree of swelling across different heating stages. Pictures were taken on the Nikon

Eclipse LV100ND optical microscope with a Nikon A1plus camera after 18 h (Plan Apo VC 20x/0.75NA DIC N2 objective from the industrial microscope CF160-2/CF160 optical system objective lens series).

2.5.11 Functionalization of films with decylamine and D-glucamine.

Unstructured and structured p(APM_{10}-*co*-AA_{90}) films on glass or polystyrene respectively were heated for 165/45. These films were then functionalized by immersion in 11.5 mM amine (Sigma Aldrich) solutions in MeOH for 24 h, followed by washing in three separate MeOH baths (soaking for 5 min each) and drying in a stream of air. To investigate the depth of functionalization, 6 wt% 165/45 heated p(APM_{10}-*co*-AA_{90}) films were submerged into solutions of fluorescein cadaverine in MeOH (0.1 mg/mL) for 24 h, followed by washing in three separate MeOH baths (soaking for 5 min each), drying in a stream of air, and visualization with a Nikon A1 Confocal Eclipse Ti microscope with Nikon A1plus camera (Plan Apo VC 20x/0.75NA).

2.5.12 Static water contact angle measurements.

Microstructured films fabricated from varying wt% of spincoating solutions (2, 4, 6, 8, 10 wt%) heat-treated for 165/45 were immediately analyzed as either: as-formed films or hydrolyzed films after submersion in PBS for 24 h and heat at 37^{o}C for 24 h to remove excess water. Video-based contact angles of the structured films were obtained using an Optical Contact Angle (OCA 35) high speed contact angle measurer (Future Digital Scientific). A drop of distilled water (5 μL) was dropped (static sessile drop method) onto

each replicate, with three replicates per sample. Video-based contact angles of the dry decylamine and D-glucamine functionalized films were obtained using an Optical Contact Angle (OCA 35) high speed contact angle measurer (Future Digital Scientific). A drop of distilled water (5 μL) was dropped (static sessile drop method) onto three different dry areas of each replicate, with three replicates per sample. Videos of the droplets were paused immediately after they landed onto the films to provide a static image which was then analyzed by the SCA20 software to determine the water contact angle.

2.5.13 Cell culturing.

NIH 3T3 *Mus musculus* (ATCC CRL-1658) fibroblasts were cultured in Dulbecco's Modified Eagle Medium (DMEM) supplemented with 10% v/v BCS and 1% v/v penicillin-streptomycin (10,000 U/mL) (Invitrogen, Life Technologies, Burlington, ON) in a 5% CO_2 environment at 37 ^{o}C with 100% humidity in a water-jacketed incubator (IncuSafe copper alloy stainless, Sanyo Scientific, Canada). Cells were washed with PBS (pH 7.4, Invitrogen, Life Technologies, Burlington, ON) and then detached using 0.25% Trypsin-EDTA (1x) phenol red and subcultured into renewed DMEM when 75-80% confluency was reached. Fibroblasts in cyrovials that were thawed from liquid nitrogen storage were allowed to passage at least two times before used for cell experiments.

2.5.14 Cell culturing for morphological and cytotoxicity assays.

All polymer films and substrates were sterilized by soaking them in 70% EtOH for 1 hour, followed by evaporation in sterile conditions. For the cell viability assay, 10,000

cells were plated onto each sample (PS, 2, 4, 6, 8, 10 wt%) and incubated for 37 ^{o}C for 22 h prior to incubation with NucBlue® Live ReadyProbes® Reagent (1 drop/sample, Invitrogen, Life Technologies, Burlington, ON) and calcein-AM solution (2 μM in PBS) from the LIVE/DEAD® Viability/Cytotoxicity Kit (Invitrogen, Life Technologies, Burlington, ON) for 30 min at room temperature before visualization on the Nikon A1 Confocal Eclipse Ti microscope with Nikon A1plus camera and Nikon Elements software (Plan Apo λ 10x/0.45NA objective). Live and dead cells were counted for each sample (n = 3 substrates) and normalized to the PS control. For the cell morphological assay on different functionalized flat films, 5000 cells were plated onto each substrate that was secured with tape on glass slides (PS, unfunctionalized, decylamine, D-glucamine) and incubated at 37 ^{o}C for 22 h prior to fixation, staining and visualization (see visualization section). For the cell morphological assay on different surface topographies, 1000 cells were plated onto each substrate (PS, flat, 2, 4, 6, 8, 10 wt%) and incubated at 37 ^{o}C for 22 h prior to fixation, staining and visualization for fractal analysis (see corresponding sections).

2.5.15 Cell fixation for morphological assays.

Following the incubation period, remaining DMEM was removed from the wells and the wells were washed with 1x PBS pH 7.4 (3x). A solution of formaldehyde (4% v/v, Sigma Aldrich) in PBS was added to each sample and incubated at room temperature for 15 minutes in the dark. The fixation solution was removed and the wells were washed with PBS (1x). Glycine (25 mM, Sigma Aldrich) in PBS was added into the wells and

incubated at room temperature for 10 minutes for quenching. The glycine solution was removed and a solution of BSA (0.2% w/v, Sigma Aldrich) and fish gelatin (0.2% w/v, Sigma Aldrich) in PBS was added. The plate was incubated for another 15 minutes at room temperature before removal and washing with PBS (1x).

2.5.16 Cell fluorescence staining and visualization for morphological assays.

DAPI (4',6-Diamidino-2-Phenylindole, Dihydrochloride) (Invitrogen, Life Technologies, Burlington, ON) and Alexa Fluor® 488 Phalloidin (Invitrogen, Life Technologies, Burlington, ON) were used to stain the nuclei and actin filaments of the fibroblasts respectively for visualization. The PBS in the wells was removed before adding DAPI (600 nM in PBS) and incubating at room temperature for 5 minutes. The DAPI solution was removed and the wells were washed with PBS (1x) before Triton^{TM} X-100 (0.2% v/v in PBS, Sigma Aldrich) was added to permeabilize the cell membranes. After 5 minutes, the substrates were washed with 1x PBS and Alexa Fluor® 488 Phalloidin (165 nM in PBS) was added for incubation at room temperature for 20 min. The staining solution was removed and replaced with PBS prior to visualization. For the cell morphological assay on different functionalized flat films, cells were imaged on a Nikon Eclipse Ti inverted microscope equipped with Nikon Elements Software (20x/0.45NA) and ANdor Zyla VSC-01598 camera. For the cell morphological assay on different surface topographies, cells were imaged using a Nikon Eclipse LV100N POL epifluorescence microscope (Nikon Instruments, Mississauga, ON) equipped with a physiological 60x/0.9NA

objective, and a Retiga 2000R camera, and NIS (Nikon Instruments, Mississauga, ON) software.

2.5.17 Fractal, cell area, and circularity analyses.

Fractal analysis was used to assess morphological differences of the fibroblasts cultured onto the structured films. The box counting method was used for fractal analysis, which involves measuring the number of different sized boxes needed to cover the perimeter or boundary of each cell. The fluorescence images of the fibroblasts were converted to a binary map after manually selecting a background from which colour intensities that were ± 2σ were rendered black, leaving the cells rendered white. The binary maps were inputted into a box counting program written in MATLAB (MathWorks) that have been used previously for fractal analysis of cells.[29] For each image, the program generates a graph of *log(N)* vs. $log(1/s^2)$, where *N* represents the number of boxes needed to cover the perimeter and *s* representing the size of the boxes (Appendix 3). The resulting graph is linear, with the slope representing the fractal dimension (F_D). Fractal dimensions corresponding to the perimeter (FDPs) of the cells were generated, with a sample size of n = 30 cells from each type of substrate. The binary maps of the cells were also inputted into ImageJ, which was used to calculate cell area and perimeter, values which were used to calculate cell circularity ($4\pi(\text{area})/(\text{perimeter})^2$) on Microsoft Excel.

2.6 Supplementary Information

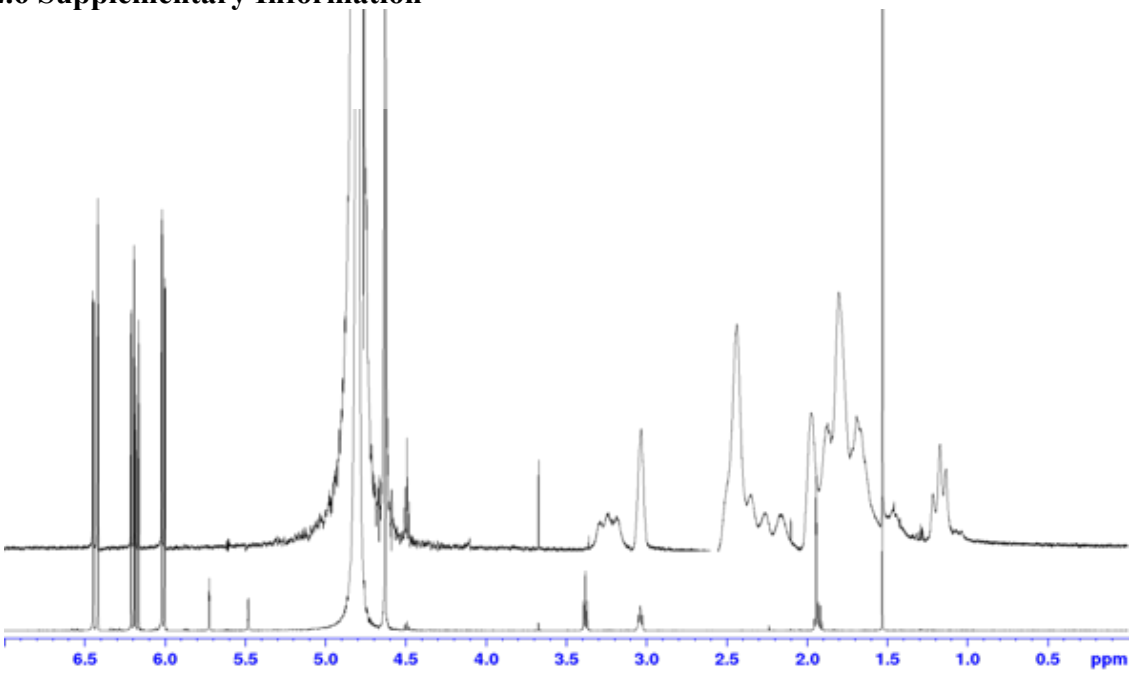

Supplementary Figure 1. ^{1}H NMR on solution a) after and b) before polymerization of p(APM-co-AA). The vinyl peaks of APM monomer at 6.45, 6.20, 6.01 ppm and AA monomer at 5.48 and 5.73 ppm, before and after polymerization, were used to calculate the monomer conversion, 92.8%.

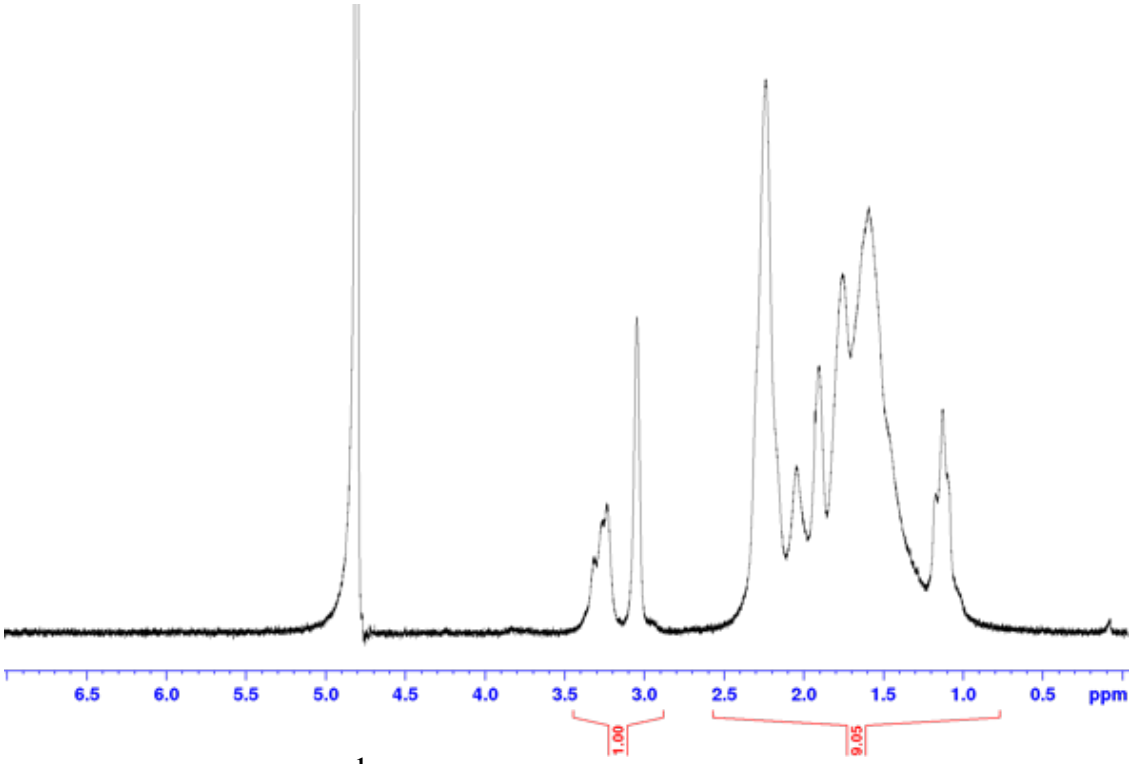

Supplementary Figure 2. ^{1}H NMR of p(APM$_{10}$-co-AA$_{90}$) after dialysis and freeze drying. The vinyl peaks are no longer present after purification, indicating there was no monomer left. The integrations of the four protons from APM at ~3.0-3.4 ppm and the nine protons from the rest of the polymer at 1.0-2.4 ppm were used to calculate the true composition of the polymer, which was 9.3% APM and 90.7% AA.

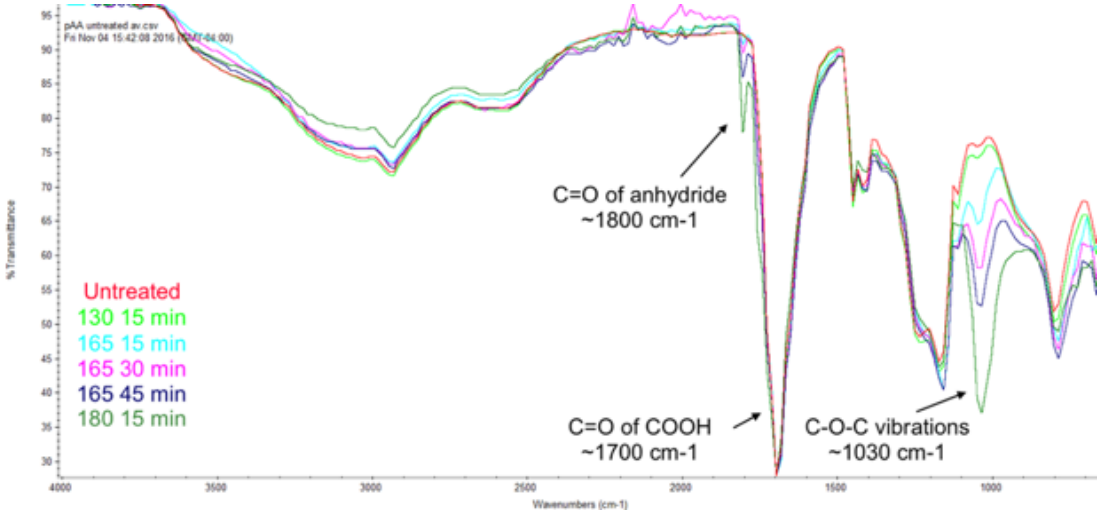

Supplementary Figure 3. ATR IR on bulk pAA heated at 130/15, 165/15, 165/30, 165/45 or 180/15. Compared to the unheated control, heated pAA spectra display two main peaks that suggest anhydride formation. After heating, the peak at 1800 cm^{-1} is likely to be from one of the C=O bonds of the anhydride, while the 1030 cm^{-1} peak is likely to be from the C-O-C bending vibration of the anhydride, previously seen in the literature.[23,24]

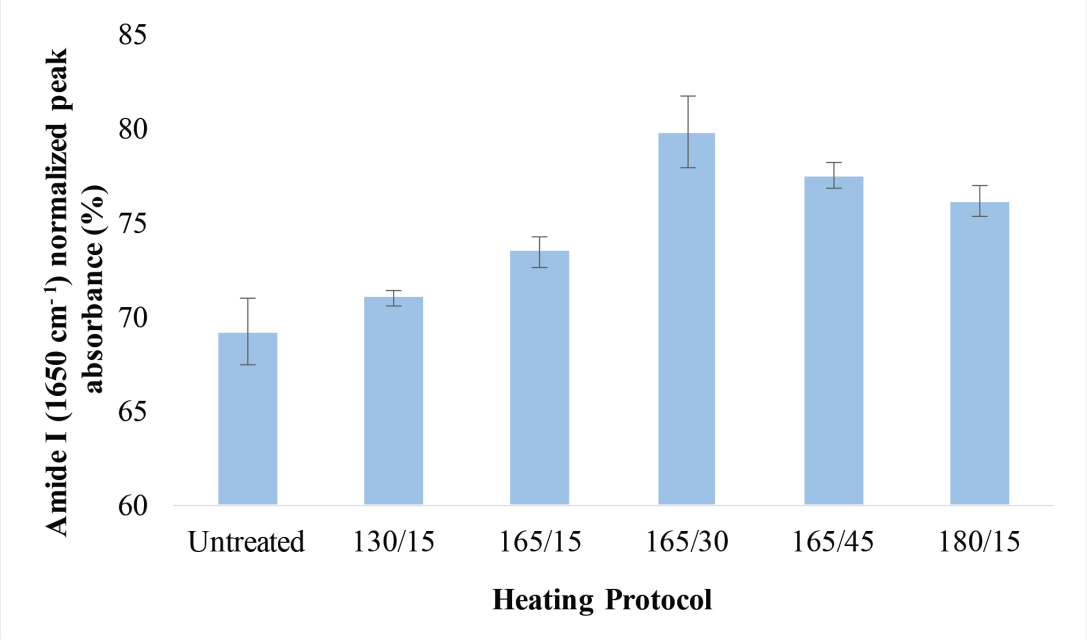

Supplementary Figure 4. Change in transmittance of the amide I peak (1650 cm^{-1}) from the ATR IR spectra on the bulk p(APM_{10}-*co*-AA_{90}) polymer heated at 130/15, 165/15, 165/30, 165/45 or 180/15. Quantitative analysis was performed on the averaged spectra by normalizing the amide I peak to the strongest peak and comparing transmittances. The percent change of the amide I peak of the 160/45 heated polymer from the unheated polymer was approximately 10%, as expected from 9.3% APM content.

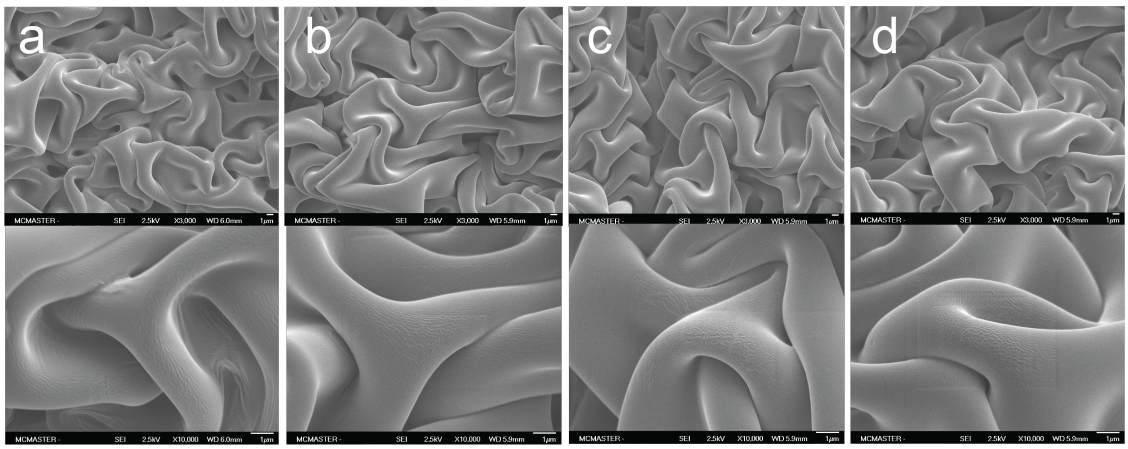

Supplementary Figure 5. SEM images of 6 wt% spincoated films on PS, heated at either a) 130/15, b) 165/15, c) 165/30, or d) 165/45. SEM was used to investigate whether there were morphological differences of the films during the different heating stages, however there were none.

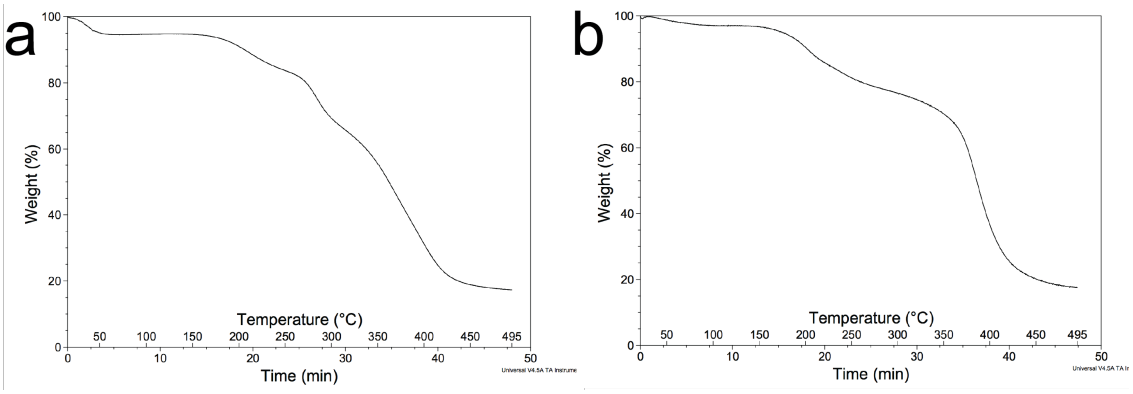

Supplementary Figure 6. TGA of a) pAA and b) p(APM$_{10}$-*co*-AA$_{90}$). A constant temperature ramp was applied (5^{o}C/min) to bulk polymer (~5 mg each) and the change in mass was measured. Degradation of either polymer probably did not occur until approximately 200^{o}C, as a significant loss of mass is seen at that temperature. This suggests that the crosslinking procedure that the system is subjected to, at 165^{o}C, does not destroy the polymer.

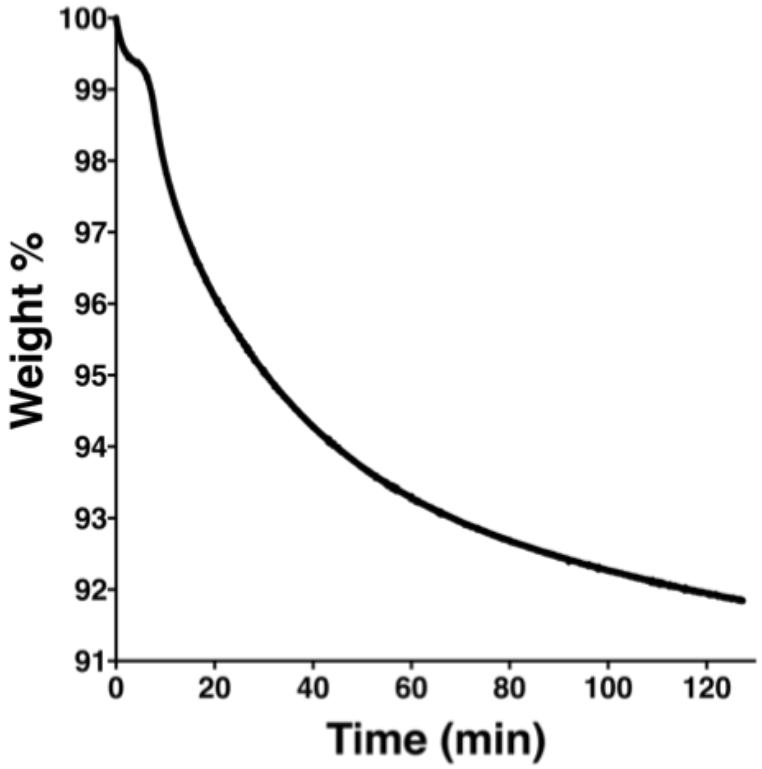

Supplementary Figure 7. Isothermal (165 °C) TGA of p(APM$_{10}$-*co*-AA$_{90}$). A constant temperature ramp was applied (10°C/min) to bulk polymer (~5 mg each) from room temperature. Weight % starting from 87 °C (during ramp) to the end of the ~2 h at 165 °C is shown. The initial mass loss was due to loss of bound water, which started to plateau at ~100°C, while the mass loss that occurred at 165°C for ~2 h was approximately ~8%, in agreement with the predicted loss of mass.

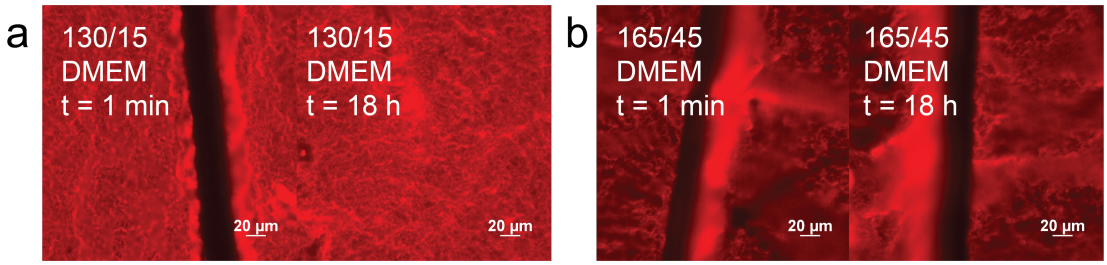

Supplementary Figure 8. Solubility tests in DMEM with BCS of a) 130/15 or b) 165/45 heated 2 wt% structured films. The films were heated and stopped at different heating stages: 130/15, 165/15, 165/30, and 165/45, and were submerged into DMEM with 10% Bovine Calf Serum (BCS).

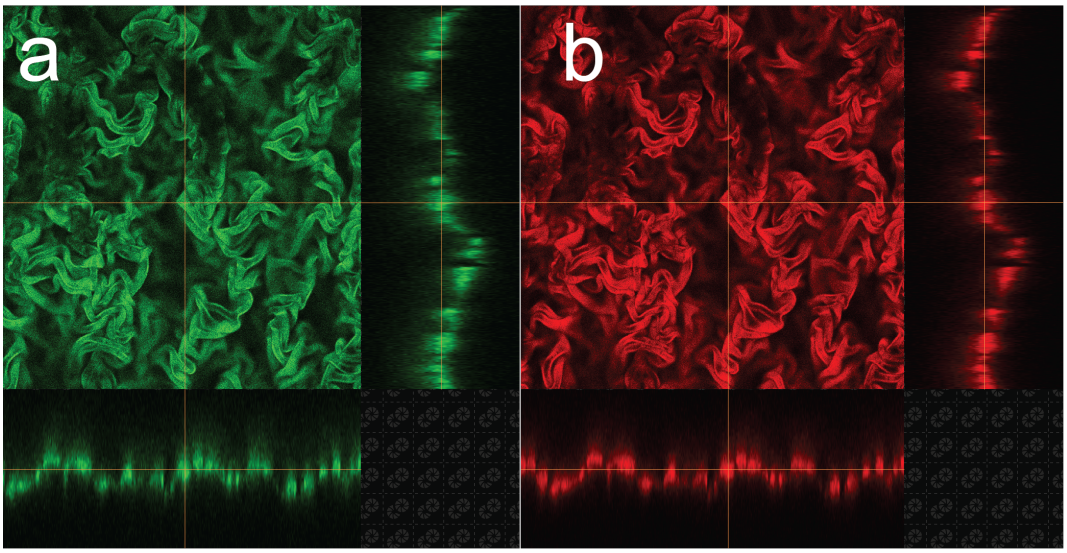

Supplementary Figure 9. a) FITC and b) TRITC channel of rhodamine labeled-p(APM$_{10}$-*co*-AA$_{90}$) films functionalized with fluorescein cadaverine. The fluorescence z-stacks of functionalized films suggest that the small molecules, such as fluorescein cadaverine, are able to penetrate through the film and functionalize the entirety of the film.

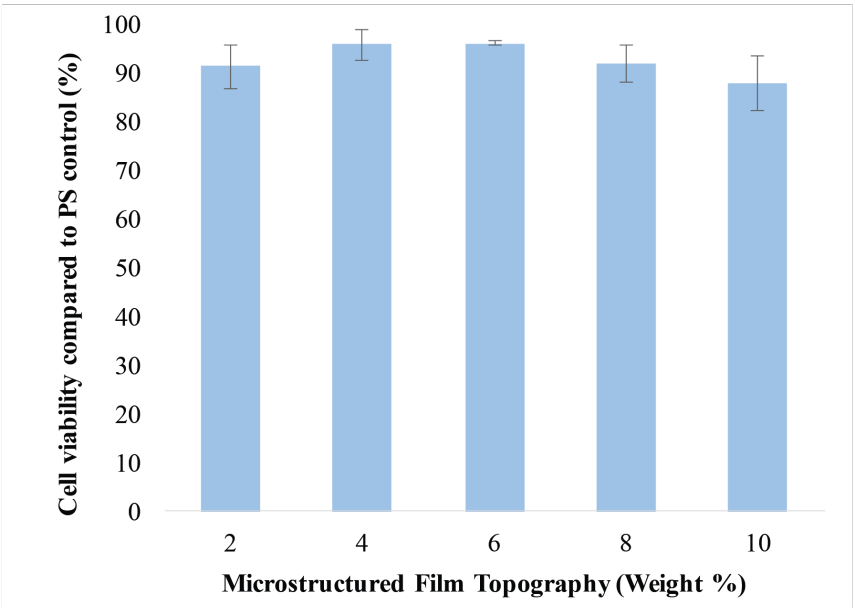

Supplementary Figure 10. Fibroblast viabilities on different weight % of microstructured films compared to tissue-culture treated polystyrene control. Cells were incubated on the microstructured films at 37°C with 5% CO_2 for 22 hours prior to incubation with NucBlue® Live ReadyProbes® Reagent and calcein-AM solution from the LIVE/DEAD® Viability/Cytotoxicity Kit for 30 minutes at room temperature before visualization on the confocal microscope. The number of alive and dead cells were quantified manually after obtaining representative images of the films (n= 38 for 10 wt%, n > 130 for 2, 4, 6, 8 wt% films).

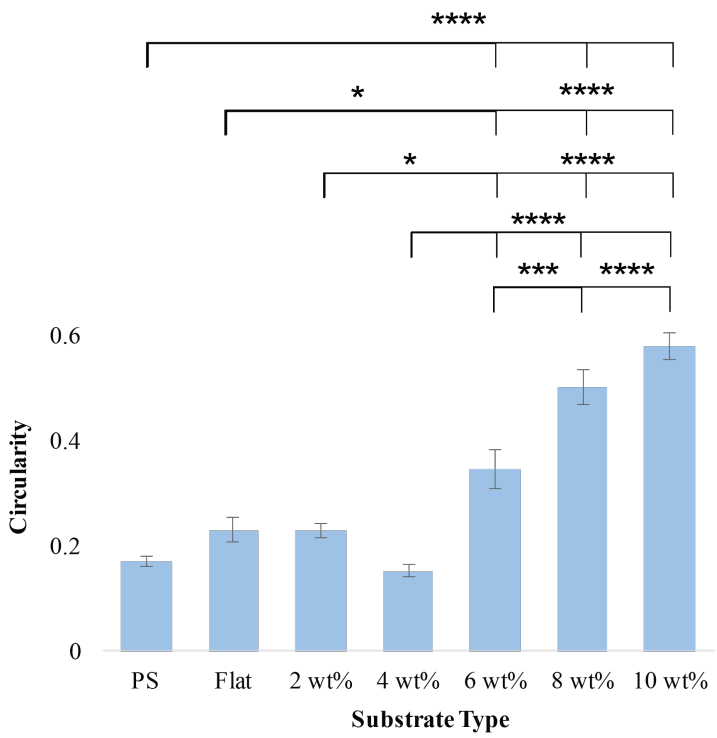

Supplementary Figure 11. Cell circularity of the fibroblasts seeded onto polystyrene, flat or different wt% structured p(APM_{10}-*co*-AA_{90}) films. Analysis of variance (ANOVA for all data sets) was performed on Prism (* = P ≤ 0.05 ** = P ≤ 0.01 *** = P ≤ 0.001**** = P ≤ 0.0001).

2.7 References

(1) Frantz, C., Stewart, K. M., and Weaver, V. M. (2010) The extracellular matrix at a glance. *J. Cell Sci. 123*, 4195–4200.

(2) Jarvelainen, H., Sainio, A., Koulu, M., Wight, T. N., and Penttinen, R. (2009) Extracellular matrix molecules: potential targets in pharmacotherapy. *Pharmacol. Rev. 61*, 198–223.

(3) Cox, T. R., and Erler, J. T. (2011) Remodeling and homeostasis of the extracellular matrix: implications for fibrotic diseases and cancer. *Dis. Model. Mech. 4*, 165–178.

(4) Schäfer, M., and Werner, S. (2008) Cancer as an overhealing wound: an old hypothesis revisited. *Nat. Rev. Mol. Cell Biol. 9*, 628–638.

(5) Venning, F. A., Wullkopf, L., and Erler, J. T. (2015) Targeting ECM disrupts cancer progression. *Frontiers in Oncology 5*, 1377.

(6) Bosman, F. T., and Stamenkovic, I. (2003) Functional structure and composition of the extracellular matrix. *J. Pathol.* (Bosman, F. T., and Stamenkovic, I., Eds.) *200*, 423–428.

(7) Butcher, D. T., Alliston, T., and Weaver, V. M. (2009) A tense situation: forcing tumour progression. *Nat. Rev. Cancer 9*, 108–122.

(8) Hughes, C. S., Postovit, L. M., and Lajoie, G. A. (2010) Matrigel: A complex protein mixture required for optimal growth of cell culture. *Proteomics 10*, 1886–1890.

(9) Kleinman, H. K., and Martin, G. R. (2005) Matrigel: Basement membrane matrix with biological activity. *Semin. Cancer Biol. 15*, 378–386.

(10) Friess, W. (1998) Collagen – biomaterial for drug delivery. *Eur. J. Pharm. Biopharm. 45*, 113–136.

(11) Johnson, K. R., Leight, J. L., and Weaver, V. M. (2007) Demystifying the effects of a three-dimensional microenvironment in tissue morphogenesis, in *Cell Mechanics*, pp 547–583. Elsevier.

(12) Lutolf, M. P., and Hubbell, J. A. (2005) Synthetic biomaterials as instructive extracellular microenvironments for morphogenesis in tissue engineering. *Nature Biotechnol. 23*, 47–55.

(13) Ehrbar, M., Rizzi, S. C., Schoenmakers, R. G., San Miguel, B., Hubbell, J. A., Weber, F. E., and Lutolf, M. P. (2007) Biomolecular hydrogels formed and degraded via site-specific enzymatic reactions. *Biomacromolecules 8*, 3000–3007.

(14) Gabardo, C. M., Zhu, Y., Soleymani, L., and Moran-Mirabal, J. M. (2013) Bench-top fabrication of hierarchically structured high-surface-area electrodes. *Adv. Funct. Mater. 23*, 3030–3039.

(15) Zhu, Y., and Moran-Mirabal, J. (2016) Highly bendable and stretchable electrodes based on micro/nanostructured gold films for flexible sensors and electronics. *Adv. Electron. Mater. 2*, 1500345.

(16) Gill, U., Sutherland, T., Himbert, S., Zhu, Y., Rheinstädter, M. C., Cranston, E. D., and Moran-Mirabal, J. M. (2017) Beyond buckling: humidity-independent measurement of the mechanical properties of green nanobiocomposite films. *Nanoscale 9*, 7781–7790.

(17) Sonney, S., Shek, N., and Moran-Mirabal, J. M. (2015) Rapid bench-top fabrication of poly(dimethylsiloxane)/polystyrene microfluidic devices incorporating high-surface-area sensing electrodes. *Biomicrofluidics 9*, 026501.

(18) Gabardo, C. M., Hosseini, A., and Soleymani, L. (2017) A new wrinkle in biosensors: wrinkled electrodes could be a breakthrough for lab-on-a-chip devices. *IEEE Nanotechnol. Mag. 10*, 6–18.

(19) Zhao, J., Burke, N. A. D., and Stöver, H. D. H. (2016) Preparation and study of multi-responsive polyampholyte copolymers of N -(3-aminopropyl)methacrylamide hydrochloride and acrylic acid. *RSC Adv. 6*, 41522–41531.

(20) Webb, K., Hlady, V., and Tresco, P. A. (1998) Relative importance of surface wettability and charged functional groups on NIH 3T3 fibroblast attachment, spreading, and cytoskeletal organization. *J. Biomed. Mater. Res. 41*, 422–430.

(21) Stewart, S. A., Backholm, M., Burke, N. A. D., and Stöver, H. D. H. (2016) Cross-linked hydrogels formed through Diels-Alder coupling of furan- and maleimide-modified poly(methyl vinyl ether- alt-maleic acid). *Langmuir 32*, 1863–1870.

(22) Chung, J. Y., Nolte, A. J., and Stafford, C. M. (2011) Surface Wrinkling: A Versatile Platform for Measuring Thin-Film Properties. *Adv. Mater. 23*, 349–368.

(23) Fyfe, C. A., and McKinnon, M. S. (1986) Investigation of the thermal degradation of poly (acrylic acid) and poly (methacrylic acid) by high-resolution carbon-13 CP/MAS NMR spectroscopy. *Macromolecules*.

(24) Eisenberg, A., Yokoyama, T., and Sambalido, E. (1969) Dehydration kinetics and glass transition of poly(acrylic acid). *J. Polym. Sci. A Polym. Chem. 7*, 1717–1728.

(25) Goujon, L. J., Hariharan, S., Sayyar, B., Burke, N. A. D., Cranston, E. D., Andrews, D. W., and Stöver, H. D. H. (2015) Tunable Hydrogel Thin Films from Reactive Synthetic Polymers as Potential Two-Dimensional Cell Scaffolds. *Langmuir 31*, 5623–

5632.

(26) Singh, A., and Elisseeff, J. (2010) Biomaterials for stem cell differentiation. *J. Mater. Chem. 20*, 8832–8847.

(27) Harvey, A. G., Hill, E. W., and Bayat, A. (2014) Designing implant surface topography for improved biocompatibility. *Expert Rev. Med. Devices 10*, 257–267.

(28) Smith, T. G., Marks, W. B., Lange, G. D., Sheriff, W. H., and Neale, E. A. (1989) A fractal analysis of cell images. *J. Neurosci. Methods 27*, 173–180.

(29) Moran-Mirabal, J. M., Aubrecht, D. M., and Craighead, H. G. (2007) Phase separation and fractal domain formation in phospholipid/diacetylene-supported lipid bilayers. *Langmuir 23*, 10661–10671.

(30) Meyle, J., Wolburg, H., and Recum, Von, A. F. (1993) Surface micromorphology and cellular interactions. *J. Biomater. Appl. 7*, 362–374.

(31) Kim, D.-H., Provenzano, P. P., Smith, C. L., and Levchenko, A. (2012) Matrix nanotopography as a regulator of cell function. *J. Cell Biol. 197*, 351–360.

(32) Stanton, M. M., Parrillo, A., Thomas, G. M., McGimpsey, W. G., Wen, Q., Bellin, R. M., and Lambert, C. R. (2014) Fibroblast extracellular matrix and adhesion on microtextured polydimethylsiloxane scaffolds. *J. Biomed. Mater. Res. 103*, 861–869.

(33) Discher, D. E., Janmey, P. A., and Wang, Y. (2005) Tissue cells feel and respond to the stiffness of their substrate. *Science 310*, 1139–1143.

(34) Berry, C. C., Campbell, G., Spadiccino, A., Robertson, M., and Curtis, A. S. G. (2004) The influence of microscale topography on fibroblast attachment and motility. *Biomaterials 25*, 5781–5788.

CHAPTER 3: ELECTROSPUN NANOFIBROUS POLYAMPHOLYTE MATS AS CELLULAR SCAFFOLDS

Christal Zhou, Jing Zhao, Kevin Saem, Jose Moran-Mirabal and Harald D. H. Stöver

3.1 Abstract

A series of polyampholytes formed by the copolymerization of *N*-(3-aminopropyl) methacrylamide hydrochloride (APM) and acrylic acid (AA), p(APM_x-*co*-AA_{100-x}), containing 6 to 35 mol% APM, were screened for electrospinning and subsequent thermally-induced self-crosslinking, and used for cell culturing. Copolymers containing 6 – 10 mol% APM could be electrospun from solutions with acidic pH, while higher APM content (20, 30, 35 mol%) largely resulted in droplet formation attributed to repulsion from excessive net charges at pH values below or above the isoelectric point (pI) and to polyampholyte chain collapse at their pI. This is the first report of successfully electrospinning synthetic polyampholytes without neutral polymeric spinning aids. The as-formed nanofibrous mats formed from p(APM_{10}-*co*-AA_{90}) were soluble in aqueous media, but could be thermally self-crosslinked through amide formation and then used as substrates for fibroblast attachment studies using fluorescence microscopy. Residual anhydride groups formed during thermal treatment may in the future be used for post-modification with amines to tune the surface chemistry of the resulting nanofibrous ECM platform.

3.2 Introduction

Cells naturally reside within an extracellular matrix (ECM) which consists of 3-dimensional (3D) networks of collagen and elastin that provide biophysical/chemical cues to direct cellular development and behaviour.[1] Studies of cell – ECM interactions often involve 2D *in vitro* models not fully representative of 3D *in vivo* conditions. Electrospinning can be used to produce polymer fibres with diameters ranging from 3 nm to > 5 μm, resulting in 3D fibrous mats that can provide both a range of interconnected pore structures and a range of fiber diameters, mimicking some features of the 3D ECM at the mesoscale.[2,3] Electrospinning involves a simple set-up comprising a conductive tip such as a metal syringe needle, a high voltage source, and a grounded collector.[3] The high electric field ionizes the polymer solution at the tip of the syringe, resulting in electrostatic repulsion within the solution and electrostatic attraction to the collector that both counteract the surface tension of the droplet at the needle tip. Once the electrostatic forces overcome this surface tension, a polymer jet is extracted from the droplet and travels towards the grounded collector. In flight, solvent evaporates and electric forces continue to stretch the jet, decreasing the diameter of the polymer fiber to the micro- to nanometer range as it deposits onto the collector.[3] An example of nanofibers produced by electrospinning includes poly(lactic-*co*-glycolic acid) (PLGA) scaffolds that exhibit high surface areas and porosities, facilitating the formation of cell attachment involving focal adhesions.[4] Natural electrospun polymeric scaffolds, such as collagen nanofibers, can also mimic the biochemical aspects of the native ECM.[5] Overall, polymer nanofibrous scaffolds, with high surface-to-volume ratios and permeability, have a wide variety of

biomedical applications, including tissue engineering scaffolds for cells to attach and grow *in vitro* prior to implantation into the body.[3]

Polyampholyte nanofiber mats can mimic ECM nanofibrous components (*i.e.,* polypeptides and proteins) in chemical composition, charge distribution, and morphology. However, it has been challenging to electrospin such highly charged polymers.[6,7] Under a high electric field, the electrostatic repulsion between ionic groups on these polymers can interfere with the formation of continuous fibers during electrospinning, leading instead to preferential formation of droplets over a wide range of polymer concentrations and electrospinning parameters.[6] The first successful electrospinning of charged polymers was reported by Park *et al.* (2004).[6] Although chitosan, a cationic polysaccharide, could not be electrospun on its own, mixtures of silk fibroin and chitosan were able to form fibers, probably due to the decreased net charge, and due to hydrogen bonding between the silk fibroin and chitosan providing additional intermolecular interactions to entangle the polymers and help form fibers.[6] Similarly, Ohkawa *et al.* (2004) successfully electrospun chitosan in aqueous solution in presence of added poly(vinyl alchohol) (PVA), which can hydrogen bond strongly with chitosan.[8] Pure chitosan could be electrospun in trifluoroacetic acid (TFA), plausibly because cationic charging by salt formation with TFA can be reversed by evaporation of the volatile TFA during fiber formation. Likewise, the addition of NaCl to the electrospinning solution of poly(2-(dimethylamino)ethyl methacrylate in its hydrochloric acid salt, helped screen the cation-cation repulsive interactions and facilitated fiber formation.[9] Mincheva *et al.* (2005) successfully electrospun N-carboxyethylchitosan, a semi-synthetic polyampholyte with a

1:2 molar ratio of [NH_2]:[COOH], into fibers in presence of added polyacrylamide or polyvinylalcohol, which are thought to enable fiber formation by hydrogen-bonding to the polyampholyte.[7] Finally, gelatin, a natural polyampholyte, cannot be electrospun in aqueous solvents due to its high charge density, but has been successfully electrospun in acidic organic solvents such as 2,2,2 trifluoroethanol and acetic acid.[10-12] In summary, electrospinning polyelectrolytes and polyampholytes requires adding either neutral polymers to promote hydrogen bonding and chain entanglement, or salts to screen repulsive charges. This work presents the successful electrospinning of a set of synthetic polyampholytes, p(APM-*co*-AA), without addition of neutral polymers as electrospinning aids.

A second challenge in developing electrospun nanofibrous mats for bio-applications involves the need to post-crosslink the fibers prior to cell culture in order to prevent excessive swelling or dissolution in aqueous media. Approaches to this challenge reported in the literature mainly involve the use of small molecule crosslinkers. For example, electrospun hydroxyapatite-containing chitosan can be crosslinked with genipin, a natural, small-molecule crosslinker that acts as a dialdehyde.[13] Other examples include electrospun gelatin nanofibers[14] and chitosan fibers[15] that were post-crosslinked with glutaraldehyde vapour. However, effective small molecule crosslinkers tend to be cytotoxic.[16] This work demonstrates thermal self-crosslinking of electrospun p(APM-*co*-AA) fibrous mats, without the use of small molecule crosslinkers. Crosslinking involves anhydrides formed from pairs of adjacent acrylic acid units reacting with primary amines on other chains to form amide crosslinks. The resulting crosslinked fibrous mats were

used for preliminary attachment studies of murine fibroblasts, using confocal fluorescence microscopy. Overall, this work describes efforts to fabricate, crosslink, and characterize electrospun fibers from a new self-crosslinkable set of polyampholytes, poly(APM_x-*co*-AA_{100-x}), as well as to study their ability to support cell culture.

3.3 Results and Discussion

3.3.1 Electrospinning p(APM-*co*-AA) to fabricate nanofibers

A series of p(APM-*co*-AA) copolymers were prepared by free radical copolymerization as reported previously,[17] and were screened under a range of conditions (*i.e.,* voltage, tip-to-collector distance, flow rate, polymer concentration, solvent, pH) for their ability to form electrospun nanofibers that could be collected as porous mats. The copolymer composition and molecular weights, as well as the associated optimized solution and electrospinning conditions, are shown in Table 3.1. Comonomer ratios were chosen to cover a series of charge ratios for the copolymers to be electrospun. The relatively high molecular weights are attributed to the facile polymerization of acrylic acid and its comonomers, and are thought to assist in chain entanglement and fiber formation. A range of polymer concentrations was explored, with only the best results being shown in Table 3.1. It is known that low polymer concentrations can favour electrospraying while high polymer concentrations can prevent jet formation.[3] Aqueous solvents, as well as mixtures of water with ethanol, methanol, or acetonitrile, were explored because of the hydrophilic nature of p(APM_x-*co*-AA_{100-x}), and because adding volatile co-solvents can promote electrospinning.[3] The pH levels of the polymer solutions were varied in order to

vary the charges on the polymer. Finally, electrospinning parameters, including voltage, tip-to-collector distance, and flow rate, were adjusted to promote Taylor cone and stable jet formation. Results indicate that p(APM-*co*-AA) compositions with 20, 30 or 35 mol% APM could not be electrospun under a wide range of parameters including low and high pH, as discussed below, whereas those containing 6 to 10 mol% APM could be electrospun with specific parameter values including low pH (Table 3.1, Figures 3.1, 3.2).

Table 3.1. Solution and Electrospinning Parameters for p(APM_x-*co*-AA_{100-x}).

mol% APM; M_w (kDa)	Polymer Weight %; [wt% NaCl]	Solvents	pH	Voltage (kV)	Distances (cm)	Flow Rates (µL/min)	Observations
35; 768	1, 2, 5	H_2O; 40:60 EtOH:H_2O	2.0; 6.4	6-20	5-10	10	Droplets (no fibers)
30; 400-700	0.2, 0.4, 0.5, 2	H_2O; 1:1 H_2O: Acetonitrile	6.0	7-20	5-11	10	Droplets (no fibers)
20; 400	3.75	20:80 MeOH: H_2O	1.2; 3.4	7.5, 8.5, 11.1	6-9	10	Droplets, a few thick fibers (>15µm)
10; 366	6.5; [2]	20:80 MeOH: H_2O	1.0; 2.9	9.5, 10.5, 11.5, 12.5	9-11.5	7, 10	Fibers, varying in size (900 nm to > 5 µm)
8; 400-700	4.1	20:80 MeOH: H_2O	2.5	8-12	9	10	Thick fibers (~2-5 µm)
6; 778	6.5	20:80 MeOH: H_2O	2.5	8-12	9	10	Thick fibers (~2-5 µm)

These observations are congruent with the literature,[6,7] as higher APM content under acidic conditions leads to increasing repulsion between positively charged APM units, which interferes with polymer entanglement and fiber formation. Analogously, at pH values above pI, repulsion from the anionic charges of the AA units together with loss of acid-acid hydrogen bonding similarly prevents entanglement and fiber formation. Finally, for pH values near the pI of each copolymer, chain collapse due to electrostatic interactions would decrease hydrodynamic volumes and hence reduce the probability of chain entanglement.[9]

Thus, solutions of p(APM-*co*-AA) with ≤ 10 mol% APM were kept at pH of 2.5 - 2.9, below the pKa of AA (4.3) and the pIs (3.2 - 3.4) of the copolymers.[17] These compositions and conditions offer acceptable net positive charge density from protonated APM, allow for hydrogen bonding between protonated carboxylic acid units, and should thus enable chain entanglement for electrospinning. Similarly, poly(acrylic acid) (pAA) has been previously electrospun at pH of ~2.3, minimizing net charge and promoting hydrogen bonding between AA units,[18] while gelatin has been electrospun in acetic acid, where it has a relatively low net cationic charge density.[11,12] Even at a low pH however, p(APM_{10}-*co*-AA_{90}) jets were not completely continuous, as droplets were still observed, which was attributed to emergence of cationic-cationic charge repulsion. Addition of 2 wt% NaCl led to decreased fibre heterogeneity for this copolymer, attributed to partial screening of the electrostatic repulsive interactions. Altogether, the composition of p(APM_x-*co*-AA_{100-x}) was the determining factor on fiber formation, as lower amounts of APM minimized repulsive cationic charges and chain collapse near the pI, and allowed more desirable acid-acid hydrogen bonding.

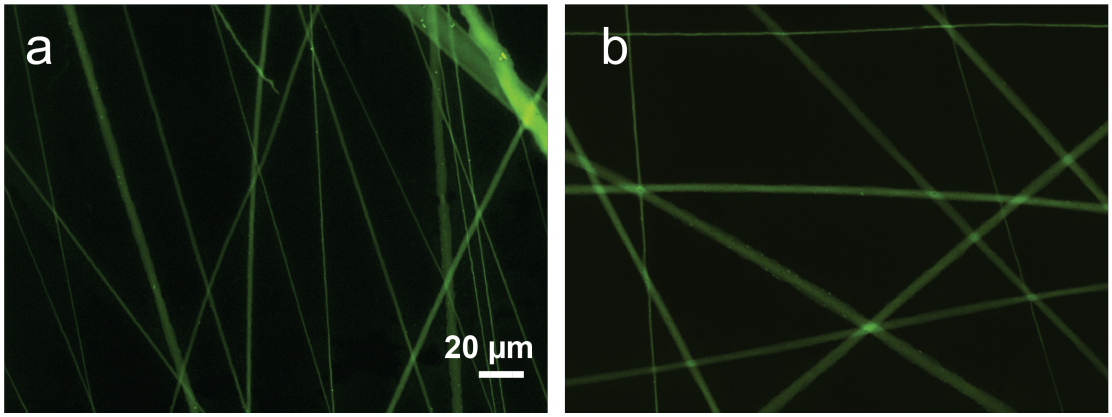

Figure 3.1. Epifluorescence images of fluorescein-doped p(APM$_8$-*co*-AA$_{92}$) and p(APM$_6$-*co*-AA$_{94}$) electrospun fibers. a) p(APM$_8$-*co*-AA$_{92}$) was electrospun at a 4.1 wt% 20:80 MeOH:H_2O polymer solution at pH ~2.5, 0.01 mL/min flow rate, 9 cm tip-to-collector distance and 11 kV, while **b)** p(APM$_6$-*co*-AA$_{94}$) was electrospun at a flow rate of 6.5 wt% 20:80 MeOH:H_2O polymer solution at pH ~2.5, 0.01 mL/min flow rate, 9 cm tip-to-collector distance and 10 kV.

Compositions of p(APM-*co*-AA) with 8, 6 and even lower APM mol% may be explored further in order to possibly generate thinner fibers, however we focussed on p(APM$_{10}$-*co*-AA$_{90}$) as its higher APM content was thought to increase the chances for successful thermal self-crosslinking post-spinning. Optimized parameters that allowed for the formation of fibers from rhodamine-labeled p(APM$_{10}$-*co*-AA$_{90}$) were: 6.5 wt% in 20:80 MeOH:H_2O at pH 2.85 with 2 wt% NaCl, 7 µL/min flow rate, 11.5 cm tip-to-collector distance, 11.5 kV, and 40-45% relative humidity (Figure 3.2a). The average diameters of the fibers obtained under these conditions were measured using a line intensity profiling method on gray scale images of the fibers and was calculated to be 1.5 ± 0.5 µm (Figure 3.2b).

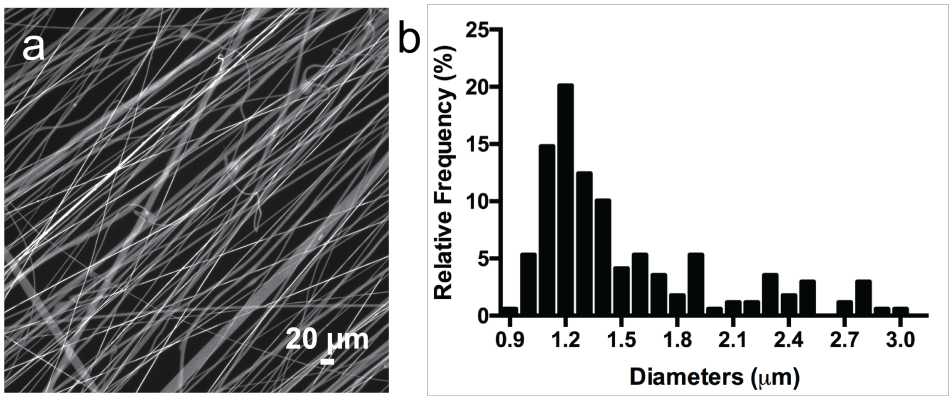

Figure 3.2. a) Epifluorescence image of p(APM$_{10}$-*co*-AA$_{90}$) nanofibers and b) histogram distribution of nanofiber diameters. The average diameters of the fibers (n = 200) were measured using a line intensity profiling method in ImageJ on epifluorescence images of the fibers (gray scale) and were calculated to be 1.5 ± 0.5 μm. Outliers were removed using ROUT (Q=1%) analysis.

3.3.2 Solubility tests on crosslinked electrospun p(APM$_{10}$-*co*-AA$_{90}$) fibers

A previous study of p(APM$_{10}$-*co*-AA$_{90}$) films (Chapter 2) had shown that thermal crosslinking through amide formation during heating to 165^{o}C was sufficient to prevent subsequent dissolution in different aqueous media. To investigate whether this process would also apply to fibrous scaffolds, p(APM$_{10}$-*co*-AA$_{90}$) fiber mats were subjected to analogous heating stages: 130/15, 165/30, and 165/45, and then submerged in Dulbecco's Modified Eagle Medium (DMEM) with 10% Bovine Calf Serum (BCS) (incubated in 5% CO_2) for 18 h. Untreated pAA (Figure 3.3d) and p(APM$_{10}$-*co*-AA$_{90}$) fibers (image not shown) dissolved immediately after submersion. Heat-treated pAA fibers dissolved slowly, probably due to the presence of hydrophobic anhydrides (image not shown). In contrast, all of the heated fibrous mats survived the solubility tests (Figure 3.3a-c). Images taken on an upright fluorescence microscope indicate, anecdotally, decreased swelling in more extensively heated fiber mats, in agreement with the expected increase

in crosslinking with heating temperature and duration. Overall, all heated copolymer fibers stayed intact after submerging in DMEM overnight, which is attributed to thermal amide crosslinking as discussed previously (Chapter 2). This crosslinking makes the nanofibers interesting candidates for applications such as biomimetic scaffolds and filtration membranes.

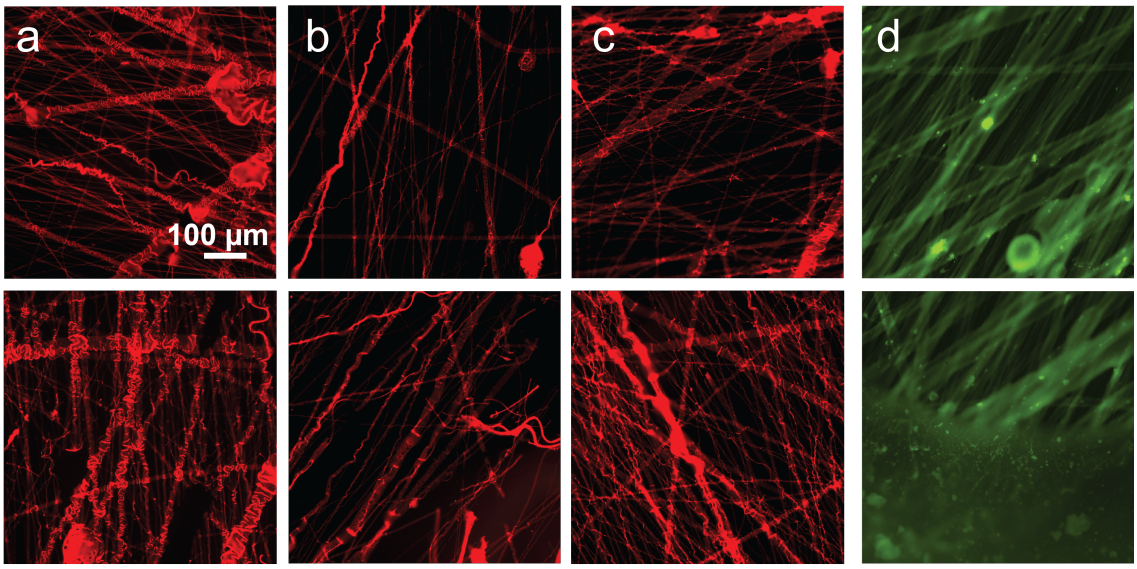

Figure 3.3. Solubility tests in DMEM with 5% CO_2 of heated p(APM_{10}-*co*-AA_{90}) (red, rhodamine labeled) and unheated pAA (green, fluorescein doped) fibers. **a)** 130/15, **b)** 165/30, and **c)** 165/45 heated p(APM_{10}-*co*-AA_{90}) fibers after 1 minute (top panel) or 18 hours (bottom panel) in DMEM with 5% CO_2 and **d)** unheated pAA fibers (top panel) immediately dissolved after a drop of DMEM was added (bottom panel). In contrast, all of the heated nanofibers survived the solubility tests. The 130/15 heated fibers displayed notable swelling overnight, possibly due to reduced heating and lowered degree of crosslinking. All images were taken at the same magnification.

3.3.3 Fibroblast attachment onto the crosslinked electrospun p(APM_{10}-*co*-AA_{90}) fibers

To investigate cellular attachment onto the p(APM_{10}-*co*-AA_{90}) fibers, 3T3 fibroblasts were seeded onto the crosslinked polymer fiber mats and incubated for 24 h in DMEM with BCS prior to cellular staining for visualization on the confocal microscope (Figure 3.4). The fibroblasts were able to attach and spread onto individual and multiple nanofibers. These observations were expected, as fibroblasts were able to attach onto the p(APM_{10}-*co*-AA_{90}) flat and structured films described earlier (Chapter 2). The highly charged surface of p(APM_{10}-*co*-AA_{90}) likely enables protein adsorption onto the surface,

allowing subsequent cell attachment.[19] It is hypothesized that more cells attach onto the nanofibers than the microstructured films due to the higher surface area available, but further work must be performed to compare cell attachment between the two different scaffold topographies. As demonstrated in the previous work involving thermally treated p(APM$_{10}$-*co*-AA$_{90}$) films, residual reactive anhydrides in the heat-treated fibers should allow for the tuning of their surface chemistry and wettability independently of fiber dimensions after crosslinking, which could be used to form a range of fibrous p(APM-*co*-AA) scaffolds for more detailed studies of cell attachment and surface responses.

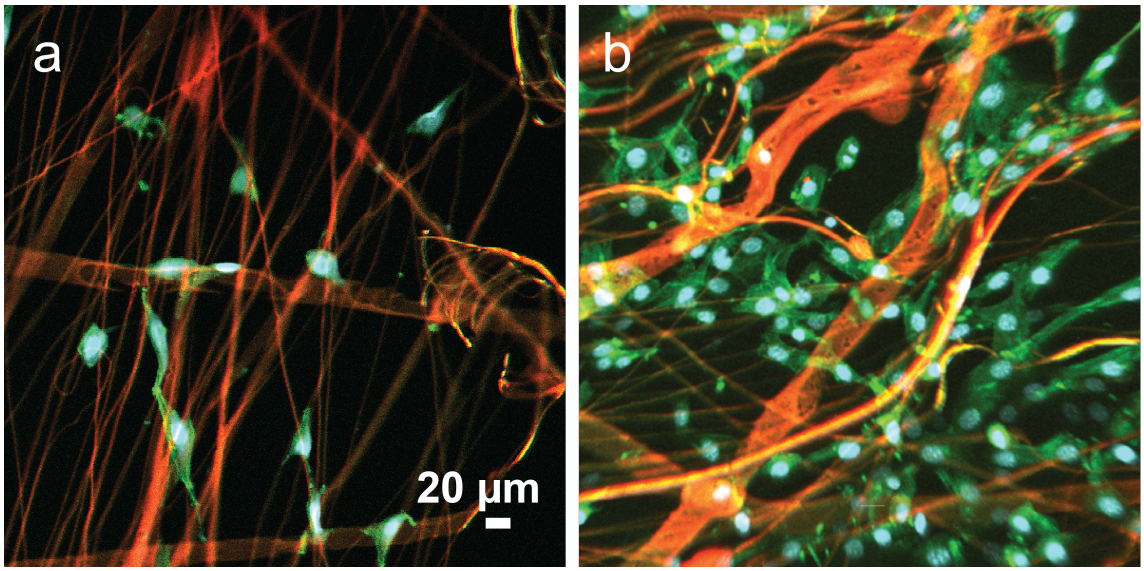

Figure 3.4. Fibroblast attachment onto crosslinked p(APM$_{10}$-*co*-AA$_{90}$) fibers. a) Confocal image of 3T3 fibroblasts that were seeded (8000 cells/sample) onto crosslinked p(APM$_{10}$-*co*-AA$_{90}$) fiber mats, which were heated at 135^{o}C for 15 minutes and 165^{o}C for 45 minutes, and incubated in DMEM with BCS for 24 hours prior to staining with DAPI and Phalloidin AlexaFluor488. **b)** 3-dimensional rendered z-stack of an image taken on confocal microscope, displayed at the same magnification.

3.4 Conclusion

A synthetic polyampholyte, p(APM_{10}-*co*-AA_{90}), was electrospun without added polymeric spinning aids, to form nanofibrous scaffolds that could be thermally crosslinked to enable use as ECM-mimetic cell scaffolds. The presence of 10 mol% APM represented an approximate upper limit for successful fiber spinning, which was attributed to increasing cation-cation electrostatic repulsion under acidic conditions, and interference from isoelectric point chain collapse or high anionic charge density at higher pH values. Fiber mats could be heat treated to induce amide crosslinking that prevented subsequent dissolution in a range of aqueous and cell culture media. The resulting crosslinked fibre mats were seeded with 3T3 fibroblasts and significant cell adhesion was observed. These preliminary experiments show the potential for these scaffolds to be used as ECM mimics in cell culture. Future work includes post-functionalizing the nanofibrous scaffolds with amine-bearing molecules to elicit different cell responses. Overall, electrospinning p(APM-*co*-AA) to fabricate nanofibers provides a new means to creating tunable, self-crosslinking, ECM-mimetic scaffolds.

3.5 Materials and Methods

3.5.1 Synthesis of p(APM_{10}-*co*-AA_{90}).

p(APM_{10}-*co*-AA_{90}) was prepared as reported previously by free radical batch-copolymerization on a 2-g scale.[17] For a 2-g scale, APM hydrochloride monomer (432 mg, Polysciences, Warrington, PA), AA monomer (1.568 g, distilled before use, 99%, Sigma Aldrich, Oakville, ON), and 2,2'-azobis(2-methylpropionamidine) dihydrochloride

(Vazo-56) (65.56 mg, 97%, Sigma Aldrich, Oakville, ON) were added to a 20 mL screw cap glass vial. Distilled water was added to the vial before placing the vial at 55^{o}C in an oven with horizontal steel rollers to rotate for 30 minutes. Ethylene carbonate (10 mg/mL, 98%, Sigma Aldrich, Oakville, ON) in D_2O (Cambridge Isotope Laboratories, Andover, MA) was used as an internal NMR integration standard. Monomer conversion was analyzed by ^{1}H NMR on a Bruker Avance 200 spectrometer at room temperature. The vinyl peaks of APM monomer at 6.45, 6.20, 6.01 ppm and AA monomer at 5.48 and 5.73 ppm, before and after polymerization, were used to calculate the monomer conversion, and the cumulative composition, calculated as 9.3% APM and 90.7% AA. Polymerized mixtures were dialyzed in distilled water using cellulose tubing (Spectra/Por, 3.5 kDa MW cutoff, Spectrum Laboratories, Rancho Dominguez, CA) for five days with two water bath changes each day. The polymer solution was then freeze-dried, which yielded 1.64 g of polymer.

3.5.2 Tagging p(APM_{10}-*co*-AA_{90}) with rhodamine B isothiocyanate.

p(APM_{10}-*co*-AA_{90}) was covalently tagged with rhodamine B isothiocyanate (0.5% labelling). Rhodamine B isothiocyanate (0.05569 g, Sigma Aldrich) was dissolved in DMF (5.6 mL, Caledon). The polymer was dissolved in 0.1 M sodium bicarbonate buffer. The pH of the solution was adjusted to 9 with NaOH (LabChem Inc, Zelienople, PA). The rhodamine B isothiocyanate solution was added dropwise into the polymer solution, which was stirred vigorously. The reaction mixture was incubated and left stirring at room temperature for 1 h. After 1 h, the pH of the solution was adjusted to pH 7 with HCl

(LabChem Inc, Zelienople, PA) to reduce swelling during dialysis. The solution was purified using dialysis against distilled water for five days, with water changes bath two times a day. The purified polymer solution was freeze-dried and yielded 1.3741 g of polymer.

3.5.3 Gel Permeation Chromatography (GPC) Analysis.

The molecular weight of the p(APM_{10}-*co*-AA_{90}) was estimated using aqueous gel permeation chromatography (GPC) setup consisting of Waters 515 HPLC pump, Waters 717 plus Autosampler, three columns (Waters Ultrahydrogel-120, -250, -500; 30 cm × 7.8 mm; 6 μm particles), and a Waters 2414 refractive index detector. The system was calibrated using narrow-dispersed PEG standards (Waters, Mississauga, ON). The mobile phase was 0.3 M $NaNO_3$ buffer. The reported M_n and M_w were 221,114 and 365,934 Da respectively, with a PDI of 1.65.

3.5.4 Fabrication of nanofibers: Electrospinning p(APM_{10}-*co*-AA_{90}).

p(APM_{10}-*co*-AA_{90}) was dissolved in a mixture of 20:80 MeOH:H_2O and the pH was adjusted to 2.8 with HCl while stirring at 37ºC for over 12 h. Solutions were used immediately for electrospinning. The solution was added to a 1 mL BD™ syringe, with a 22 G needle and seated onto a syringe pump. An alligator clip connected to a power supply (0-20 kV) was attached onto the needle. A rotating metal collector was used, which made contact with wires attached to the power supply. The tip-to-collector distance was 11.5 cm. Electrospinning was performed at a flow rate of 7 μL/min, 11.5 kV voltage

and 40-45% humidity for 30 min. Polymer was electrospun onto glass cover slips that were taped onto the rotating metal collector.

3.5.5 Visualization of fibers.

Nanofibers were visualized using a Nikon Eclipse LV100ND optical microscope equipped with an Andor Zyla sCMOS camera and NIS Elements software. The average diameters of the fibers (n = 200) were measured using a line intensity profiling method on ImageJ, where the line tool and a full width at half maximum plugin (FWHM_line plugin obtained from John Lim, Institute of Medical Biology, https://www.a-star.edu.sg/imb/Tech-Platforms/IMB-Microscopy-Unit/People.aspx) was used to obtain line intensity profiles and the full width at half maximum values, which represent the fiber diameters. GraphPad Prism (GraphPad software, CA, USA) was used to identify outliers using a ROUT (Q=1%) outlier test prior to plotting the data into a histogram.

3.5.6 Solubility Tests in Dulbecco's Modified Eagle Medium (DMEM).

Films that were heated for either 130/15, 165/15, 165/30, or 165/45 were submerged into either DMEM with 10% BCS (Invitrogen, Life Technologies, Burlington, ON) and incubated with 5% CO_2 to mimic physiological conditions or water containing 1 mM NaOH (immediately or 18 h after submersion) to investigate the structural integrity and degree of swelling across different heating stages. Nanofibrous scaffolds in 1 mM NaOH delaminated and thus were not shown, however images indicate that they did not dissolve. Images of the films under DMEM with 10% BCS were taken on the Nikon Eclipse

LV100ND optical microscope with a Nikon A1plus camera after 18 h (Plan Apo VC 20x/0.75NA DIC N2 objective from the industrial microscope CF160-2/CF160 optical system objective lens series).

3.5.7 Cell culturing.

NIH 3T3 *Mus musculus* (ATCC CRL-1658) fibroblasts were cultured in Dulbecco's Modified Eagle Medium (DMEM) supplemented with 10% v/v BCS and 1% v/v penicillin-streptomycin (10,000 U/mL) (Invitrogen, Life Technologies, Burlington, ON) in a 5% CO_2 environment at 37 ^{o}C with 100% humidity in a water-jacketed incubator (IncuSafe copper alloy stainless, Sanyo Scientific, Canada). Cells were washed with PBS (pH 7.4, Invitrogen, Life Technologies, Burlington, ON) and then detached using 0.25% Trypsin-EDTA (1x) phenol red and subcultured into renewed DMEM when 75-80% confluency was reached. Fibroblasts in cyrovials that were thawed from liquid nitrogen storage were allowed to passage at least two times before used for cell experiments.

3.5.8 Cell culturing for cell attachment assay.

Polymer nanofibrous mats were sterilized by soaking them in 70% EtOH for 1 hour, followed by evaporation in sterile conditions. 8000 cells were plated onto the nanofibrous mats (n=3) and incubated at 37^{o}C for 24 h prior to fixation, staining and visualization (see corresponding sections).

3.5.9 Cell fixation.

Following the incubation period, remaining DMEM was removed from the wells and the wells were washed with 1x PBS pH 7.4 (3x). A solution of formaldehyde (4% v/v, Sigma Aldrich) in PBS was added to each sample and incubated at room temperature for 15 minutes in the dark. The fixation solution was removed and the wells were washed with PBS (1x). Glycine (25 mM, Sigma Aldrich) in PBS was added into the wells and incubated at room temperature for 10 minutes to quench the fixation reaction. The glycine solution was removed and a solution of BSA (0.2% w/v, Sigma Aldrich) and fish gelatin (0.2% w/v, Sigma Aldrich) in PBS was added. The plate was incubated for another 15 minutes at room temperature before removal and washing with PBS (1x).

3.5.10 Cell fluorescence staining and visualization.

DAPI (4',6-Diamidino-2-Phenylindole, Dihydrochloride) (Invitrogen, Life Technologies, Burlington, ON) and Alexa Fluor® 488 Phalloidin (Invitrogen, Life Technologies, Burlington, ON) were used to stain the nuclei and actin filaments of the fibroblasts respectively for visualization. The PBS in the wells was removed before adding DAPI (600 nM in PBS) and incubating at room temperature for 5 minutes. The DAPI solution was removed and the wells were washed with PBS (1x) before Triton^{TM} X-100 (0.2% v/v in PBS, Sigma Aldrich, Oakville, ON) was added to permeabilize the cell membranes. After 5 minutes, the substrates were washed with 1x PBS and Alexa Fluor® 488 Phalloidin (165 nM in PBS) was added for incubation at room temperature for 20 min. The staining solution was removed and replaced with PBS prior to visualization with a

Nikon A1 Confocal Eclipse Ti microscope with Nikon A1plus camera and Nikon Elements software (Plan Apo λ 4x/0.2NA objective).

3.6 References

(1) Frantz, C., Stewart, K. M., and Weaver, V. M. (2010) The extracellular matrix at a glance. *J. Cell Sci. 123*, 4195–4200.

(2) Xu, C., Inai, R., Kotaki, M., and Ramakrishna, S. (2004) Electrospun nanofiber fabrication as synthetic extracellular matrix and its potential for vascular tissue engineering. *J. Tissue Eng. 10*, 1160–1168.

(3) Pham, Q. P., Sharma, U., and Mikos, D. A. G. (2006) Electrospinning of polymeric nanofibers for tissue engineering applications: a review. *J. Tissue Eng. 12*, 1197–1211.

(4) Li, W. J., Laurencin, C. T., Caterson, E. J., Tuan, R. S., and Ko, F. K. (2002) Electrospun nanofibrous structure: A novel scaffold for tissue engineering. *J. Biomed. Mater. Res. 60*, 613–621.

(5) Matthews, J. A., Wnek, G. E., Simpson, D. G., and Bowlin, G. L. (2002) Electrospinning of collagen nanofibers. *Biomacromolecules 3*, 232–238.

(6) Park, W. H., Jeong, L., Yoo, D. I., and Hudson, S. (2004) Effect of chitosan on morphology and conformation of electrospun silk fibroin nanofibers. *Polymer 45*, 7151–7157.

(7) Mincheva, R., Manolova, N., Paneva, D., and Rashkov, I. (2005) Preparation of polyelectrolyte-containing nanofibers by electrospinning in the presence of a non-ionogenic water-soluble polymer. *J. Bioact. Compat. Polym. 20*, 419–435.

(8) Ohkawa, K., Cha, D., Kim, H., Nishida, A., and Yamamoto, H. (2004) Electrospinning of chitosan. *Macromol. Rapid Commun. 25*, 1600–1605.

(9) Matthew G McKee, Matthew T Hunley, John M Layman, A., and Long, T. E. (2005) Solution rheological behavior and electrospinning of cationic polyelectrolytes. *Macromolecules 39*, 575–583.

(10) Huang, Z. M., Zhang, Y. Z., Ramakrishna, S., and Lim, C. T. (2004) Electrospinning and mechanical characterization of gelatin nanofibers. *Polymer 45*, 5361–5368.

(11) Erencia, M., Cano, F., Tornero, J. A., Fernandes, M. M., Tzanov, T., Macanás, J., and Carrillo, F. (2015) Electrospinning of gelatin fibers using solutions with low acetic acid concentration: Effect of solvent composition on both diameter of electrospun fibers and cytotoxicity. *J. Appl. Polym. Sci. 132*, DOI: 10.1002–app.42115.

(12) Tonsomboon, K., Butcher, A. L., and Oyen, M. L. (2017) Strong and tough nanofibrous hydrogel composites based on biomimetic principles. *Mater. Sci. Eng. C. 72*, 220–227.

(13) Frohbergh, M. E., Katsman, A., Botta, G. P., Lazarovici, P., Schauer, C. L., Wegst, U. G. K., and Lelkes, P. I. (2012) Electrospun hydroxyapatite-containing chitosan nanofibers crosslinked with genipin for bone tissue engineering. *Biomaterials 33*, 9167–9178.

(14) Zhang, Y. Z., Venugopal, J., Huang, Z. M., Lim, C. T., and Ramakrishna, S. (2006) Crosslinking of the electrospun gelatin nanofibers. *Polymer 47*, 2911–2917.

(15) Schiffman, J. D., and Schauer, C. L. (2007) Cross-linking chitosan nanofibers. *Biomacromolecules 8*, 594–601.

(16) Gough, J. E., Scotchford, C. A., and Downes, S. (2002) Cytotoxicity of glutaraldehyde crosslinked collagen/poly(vinyl alcohol) films is by the mechanism of apoptosis. *J. Biomed. Mater. Res. 61*, 121–130.

(17) Zhao, J., Burke, N. A. D., and Stöver, H. D. H. (2016) Preparation and study of multi-responsive polyampholyte copolymers of N -(3-aminopropyl)methacrylamide hydrochloride and acrylic acid. *RSC Adv. 6*, 41522–41531.

(18) Li, L., and Hsieh, Y.-L. (2005) Ultra-fine polyelectrolyte fibers from electrospinning of poly(acrylic acid). *Polymer 46*, 5133–5139.

(19) Webb, K., Hlady, V., and Tresco, P. A. (1998) Relative importance of surface wettability and charged functional groups on NIH 3T3 fibroblast attachment, spreading, and cytoskeletal organization. *J. Biomed. Mater. Res. 41*, 422–430.

CHAPTER 4: Conclusion and Future Directions

4.1 Conclusion

In this work, a well-characterized polyampholyte system, p(APM-*co*-AA), was used to construct two types of scaffolds, microstructured films and nanofibrous mats, to be potentially used as ECM mimics. For the first time, ATR IR was used to confirm that p(APM-*co*-AA) can be crosslinked under heat without the use of small molecule cross-linkers. In addition, the crosslinked films and fibers were subjected to solubility tests under DMEM and 1 mM NaOH, which confirmed their structural integrity in solution. The ability to self-crosslink eliminates the need for chemical post-processing, improving biocompatibility and allowing the scaffolds to possess sufficient mechanical integrity to be used in cell culturing conditions. The surface wettabilities of the flat and microstructured films were successfully modified by functionalizing the films with either decylamine or D-glucamine, which elicited different cell morphologies, demonstrating the chemical tunability of the polymer scaffolds. The chemical tunability of these scaffolds presents another advantage, as small molecules can be used to easily functionalize these scaffolds and cause changes in cell behaviour that can be studied. Fractal analysis on the cell perimeters of murine fibroblasts seeded onto microstructured films of varying topographies suggest that larger structures contributed to more circular cell shapes and decreased cell areas, which may be more representative of *in vivo* morphologies.[1] The ability to tune surface topography using flat film thickness provides another tunable property that can be used to elicit varying cell responses, possibly ranging from growth, apoptosis and differentiation. Cell viability tests also confirmed the non-

cytotoxicity of the microstructured polymer films. Furthermore, this work presents the use of electrospinning for the formation of nanofibrous mats from this polyampholyte for the first time, confirming the challenges encountered in the literature when electrospinning charged polymers. Future work will include electrospinning copolymer polyampholytes that do not undergo chain collapse at their pH(I), to expand the suite of polyampholyte-based nanofibrous mats. Overall, the composition, surface chemistry, and wettability of the p(APM-*co*-AA) system can be easily tuned, making it a great candidate as ECM-mimic scaffolds to study cell morphology, adhesion, and behaviour *in vitro*. These tunable p(APM-*co*-AA) polyampholyte scaffolds can be both electrospun into nanofibers and used to fabricate microstructured polymer films, adding another tool in the field of biomimetic ECM scaffolds to study, probe, and understand the ECM in a wide range of applications such as biomedical and regenerative medicine research.

4.2 Future Directions

Future experiments with the p(APM-*co*-AA) scaffolds include investigating other compositions of p(APM-*co*-AA) to determine whether the degree of crosslinking can be tuned using composition, as less or more APM could potentially allow for different crosslinking capacities. Changing the degree of crosslinking can result in varying the elastic moduli of the scaffolds, be another property that can be used to study other aspects of cell behaviour including stem cell differentiation and proliferation, which depend on surface stiffness.[2] For example, Leipzig *et al.* found that neuronal stem cell differentiation is favored on softer surfaces while oligodendrocyte differentiation is favored on stiffer scaffolds.

Furthermore, the electrospun p(APM-*co*-AA) scaffolds could be explored further by investigating the functionalization of the nanofibers after heating. Small molecules other than decylamine and D-glucamine could be grafted onto the nanofibrous or microstructured scaffolds to elicit specific cell behaviour. The chemical environment and hydrophilicity of tissue engineering scaffolds can have profound effects on cell adhesion and function.[3] For example, Benoit *et al.* demonstrated that small-molecule chemical functional groups, such as 2-aminoethyl methacrylate, *t*-butyl methacrylate or ethylene glycol methacrylate phosphate, functionalized onto poly(ethylene glycol) (PEG) were able to induce differentiation of human mesenchymal stem cells. Furthermore, the surface chemistry can be tuned to mediate cell responses through integrins, cell transmembrane receptors responsible for cell-ECM and cell-cell adhesion.[4] For example, soluble or immobilized agents, such as angiostatin, can inhibit integrin function and reduce

thrombosis or inflammatory responses associated with biomaterial implants by preventing leukocyte recruitment.[5,6] Overall, the presence of anhydride groups in the p(APM-*co*-AA) system allow for the post-functionalization of the crosslinked nanofibers, which could be explored further with different small molecules to study specific cell responses.

Extensions to this project include incorporating polymer hydrogel microspheres onto the microstructured films and nanofibrous scaffolds. Microspheres comprised of poly(4-methylstyrene-*alt*-maleic anhydride) (3-20 μm) have been synthesized and previously explored in fabricating 3D cellular scaffolds.[7] A challenge encountered while using microspheres as cellular scaffolds is creating scaffolds with sufficient pore interconnectivity and structural integrity, properties that are required for proper cell attachment and migration.[7,8] This can be difficult as individual microspheres may not be able to self-assemble into structures with interconnectivity for cells to attach onto.[7] Our p(APM-*co*-AA) nanofibrous or microstructured scaffolds can act as platform onto which net cationic (e.g. tetraethylenepentamine functionalized), anionic (e.g hydrolyzed), or anhydride polymer microspheres can ionically or covalently attach in aqueous or organic solvents (e.g. DMF) respectively, allowing for increased interconnectivity and surface area for cells to bind. The polymer microspheres can also act as cell mimics in an environment that mimics the ECM, as their diameters are comparable to cell sizes, ranging from 3-20 μm.[7] Microsphere diameters can be easily tuned by varying the amount of crosslinker, which is important in ensuring they can fit into the microstructured film structures and nanofibrous mats. Kim *et al*. (2017) demonstrated that fibroblasts that were co-encapsulated with microspheres showed improved survival compared to

without.[9] The co-encapsulated microspheres provided surfaces for the fibroblasts to adhere onto and proliferate, leading to higher viability and growth. Overall, incorporating microspheres onto our nanofibrous or microstructured scaffolds may increase surface area for protein adsorption and cell adhesion sites, which may improve the long-term survival and growth of cells that are seeded onto the scaffolds.

Polyelectrolytes can be used to fabricate electrically responsive hydrogels in applications such as controlled drug delivery.[10,11,12] For example, hydrogels based on chitosan and poly(hydroxyethyl methacrylate) show piezoelectric behaviour,[11] and polyacrylamide-*g*-alginate-based hydrogels demonstrated increased drug release upon the introduction of an electric stimulus.[10] In addition, combinations of agarose and other anionic polymers, such as xanthan gum, could potentially be used as drug delivery systems as well.[12] The proposed mechanism in the electrical responses from polyelectrolyte hydrogels involves the formation of hydrogen ions near the anode, which protonates anionic groups and causes the hydrogel to collapse, expelling water to release small molecules from the hydrogel.[12] p(APM_{10}-*co*-AA_{90}) microstructured films, which are net anionic at physiological conditions, could potentially exhibit sensitivity to electric stimuli and be a vehicle for drug delivery, as small molecules are able to penetrate through the nanofibrous and microstructured films.

Another possible application of polyampholyte scaffolds include use as antimicrobial surfaces when studying cell behaviour. Microbial infection is also a major problem in medical devices, drugs, health care, and food storage.[13] Antimicrobial polymers have recently received increased attention, as they show promise as

antimicrobial agents while reducing the environmental problems of conventional antimicrobial agents. For example, polymer quaternary ammonium salts (QAS) can exhibit higher antimicrobial activities than small molecule QASs, which have been widely used as antimicrobial agents.[14] Zhang *et al.* synthesized acrylamide polymers containing QASs, including (2-methacrylamido) propyltetrabutyldimethylammonium bromide, which demonstrated antimicrobial activities on bacteria and phytopathogenic fungi.[14] QAS units could be incorporated into the p(APM-*co*-AA) backbone for potential antimicrobial properties. p(APM-*co*-AA-*co*-QAS) scaffolds, possibly demonstrating antimicrobial properties, could be used to study cell or microbial behaviour. Alternatively, the p(APM-*co*-AA) system could be functionalized with QAS molecules after crosslinking. Overall, the chemical and physical tunability of these self-crosslinking p(APM-*co*-AA) polyampholytes allow them to potentially be applied in a variety of applications, including as cellular scaffolds, drug delivery, and antimicrobial surfaces.

4.3 References

(1) Stanton, M. M., Parrillo, A., Thomas, G. M., McGimpsey, W. G., Wen, Q., Bellin, R. M., and Lambert, C. R. (2014) Fibroblast extracellular matrix and adhesion on microtextured polydimethylsiloxane scaffolds. *J. Biomed. Mater. Res. 103*, 861–869.

(2) Leipzig, N. D., and Shoichet, M. S. (2009) The effect of substrate stiffness on adult neural stem cell behavior. *Biomaterials 30*, 6867–6878.

(3) Benoit, D. S. W., Schwartz, M. P., Durney, A. R., and Anseth, K. S. (2008) Small functional groups for controlled differentiation of hydrogel-encapsulated human mesenchymal stem cells. *Nat. Mater. 7*, 816–823.

(4) Hynes, R. O. (2002) Integrins: Bidirectional, allosteric signaling machines. *Cell 110*, 673–687.

(5) García, A. J. (2005) Get a grip: integrins in cell–biomaterial interactions. *Biomaterials 26*, 7525–7529.

(6) Chavakis, T., Athanasopoulos, A., Rhee, J.-S., Orlova, V., Schmidt-Wöll, T., Bierhaus, A., May, A. E., Celik, I., Nawroth, P. P., and Preissner, K. T. (2005) Angiostatin is a novel anti-inflammatory factor by inhibiting leukocyte recruitment. *Blood 105*, 1036–1043.

(7) Zhou, C., and Stöver, H. D. H. (2016) Functionalization and characterization of poly(4-methylstyrene-alt-maleic anhydride) microspheres as potential 3D cell scaffolds. Undergraduate Thesis. McMaster University, Hamilton, ON.

(8) Lee, J., Cuddihy, M. J., and Kotov, N. A. (2008) Three-dimensional cell culture matrices: state of the art. *Tissue Eng. Part B Rev. 14*, 61–86.

(9) Kim, I.-Y., Choi, H., and Kim, K. K. (2017) Improved survival of anchorage-dependent cells in core-shell hydrogel microcapsules via co-encapsulation with cell-friendly microspheres. *J. Microencapsul. 34*, 57–62.

(10) Kulkarni, R. V., Setty, C. M., and Sa, B. (2010) Polyacrylamide-g-alginate-based electrically responsive hydrogel for drug delivery application: Synthesis, characterization, and formulation development. *J. Appl. Polym. Sci. 115*, 1180–1188.

(11) Kim, S. J., Shin, S. R., Lee, S. M., Kim, I. Y., and Kim, S. I. (2004) Electromechanical properties of hydrogels based on chitosan and poly(hydroxyethyl methacrylate) in NaCl solution. *Smart Mater. Struct. 13*, 1036–1039.

(12) Hsu, C.-S., and Block, L. H. (1996) Anionic gels as vehicles for electrically-modulated drug delivery. i. Solvent and drug transport phenomena. *Pharm. Res. 13*,

1865–1870.

(13) Kenawy, E.-R., Worley, S. D., and Broughton, R. (2007) The chemistry and applications of antimicrobial polymers: A state-of-the-art review. *Biomacromolecules 8*, 1359–1384.

(14) Zhang, A., Liu, Q., Lei, Y., Hong, S., and Lin, Y. (2015) Synthesis and antimicrobial activities of acrylamide polymers containing quaternary ammonium salts on bacteria and phytopathogenic fungi. *React. Funct. Polym. 88*, 39–46.